

Camber and flap effects in the dynamic aeroelastic analysis of the typical aerofoil section

Joseba Murua



Imperial College London
Department of Aeronautics

September 13, 2008

Acknowledgments

I would like to acknowledge Dr. Peirò and Dr. Palacios for their help in the development of this project. Their experience and knowledge has greatly helped towards the achievement of the objectives of this work.

I would also like to show my gratitude to my family, Rubén and Naiara for their support, understanding, patience and love.

Finally, I would like to thank Fundación Caja Madrid for awarding the scholarship that has allowed me not only to study this MSc, but to pursue further objectives.

IMPERIAL COLLEGE LONDON
AERONAUTICS DEPARTMENT LIBRARY
TEL: 0207 5945069

STANDARD LOAN

Please return by the date below. Loan periods may be shortened if items are reserved by other users. Failure to return reserved items on time will result in a fine.

--	--	--



2406757073

Abstract

In classical aeroelasticity, the typical flat plate section consists of two degrees of freedom, namely pitch and plunge. Current resources offer the capability of enhancing the response of the typical aerofoil by making it adaptive. This project investigates the dynamic aeroelastic effects of two of these options: trailing edge flaps and chordwise (camber) deformations.

The structural model is assumed to be linear and damping is neglected. For the aerodynamic loads linear unsteady theory has been used, implementing Theodorsen's theory and Wagner's indicial response method. From the resulting equations of motion, flutter speed has been computed by several procedures, both in the frequency domain (V-g method and stability of linear state-space systems) and time domain.

In the case of the trailing edge flap, it has been proved that some results provided by Theodorsen [1] and Theodorsen and Garrick [2] were in error, as it had been previously reported by Zeiler [3]. In addition, a parametric study has been carried out in order to study the influence of the parameters of the flat plate on the flutter speed. The stability boundary presents an important dip in the neighbourhood of $\frac{\omega_\beta}{\omega_\alpha} = 1$ and most of the characteristic parameters only translate or scale this boundary. However, the natural frequency ratio $\frac{\omega_h}{\omega_\alpha}$ plays a very important role and it can change the shape of the curve completely. The mass ratio κ is also critical, since the characteristic dip can be softened to a extent where the minimum flutter velocity is nearly the same as the average value along the whole span of $\frac{\omega_\beta}{\omega_\alpha}$.

The inclusion of the camber degree of freedom in flutter analysis represents a novelty. Although different models for chordwise deformation had been proposed [4], [5], [6] and [7], stability analysis has never been undertaken before. The model for camber is taken from Palacios and Cesnik [7] and aided by V-g plots and eigenvector analysis, mechanisms driving flutter have been explained for one, two and three degrees-of-freedom systems that include camber.

Unlike classical degrees of freedom pitch and plunge, camber mode alone can lead to flutter. Critical velocity always happens at the same reduced frequency k , being the camber-wake interaction responsible for instability. This is contrary to pitch and plunge modes, where only interaction of both modes can cause flutter. Pitch-camber and plunge-camber systems exhibit regions where camber-wake interaction governs flutter, apart from where mode interaction prevails. In the case of three degrees of freedom, it has been found that the triple interaction among modes is crucial, as it dominates over a broad range of natural frequency ratios. Static divergence is also very important, since there are regions where it occurs before flutter speed is reached.

Nomenclature

$A(k)$	complex matrix of aerodynamic coefficients
A_i	coefficients of exponential representation of Wagner function
a	coordinate of elastic axis in semi-chords
b	semi-chord
b_i	exponents of exponential representation of Wagner function
C_H	flap hinge moment coefficient
C_L	lift coefficient
C_Λ	bimoment coefficient
C_M	moment coefficient
c	flap hinge location in semi-chords
G	shear modulus
g_i	fictitious structural damping for the V-g method for flutter
$k = \frac{b\omega}{V}$	reduced frequency
H	hinge moment
L	lift
Λ	bimoment
M	moment
m	mass of aerofoil per unit length
$q_\infty = \frac{1}{2}\rho_\infty V_\infty^2$	free-stream dynamic pressure
\mathbf{r}	vector storing the degrees of freedom: α, h, β, δ
$s = \frac{Vt}{b}$	non-dimensional time
t	physical time
t_p	thickness of plate
V_∞	free-stream velocity
w	vertical displacement
z_i	aerodynamic states for Leishman's state-space formulation
I_α	moment of inertia of aerofoil-flap around elastic axis, per unit span
I_β	moment of inertia of flap around hinge, per unit span
I_δ	moment of inertia of camber, per unit span
K_α	torsional stiffness of aerofoil-flap around elastic axis, per unit span
K_β	torsional stiffness of flap around hinge, per unit span
K_δ	camber stiffness, per unit span
K_h	plunge stiffness, per unit span
S_α	static moment of aerofoil-flap around elastic axis, per unit span
S_β	static moment of flap around hinge, per unit span

$r_\alpha = \sqrt{\frac{I_\alpha}{mb^2}}$	radius of gyration aerofoil-flap referred to a
$r_\beta = \sqrt{\frac{I_\beta}{mb^2}}$	reduced radius of gyration of flap referred to c
$\omega_\alpha = \sqrt{\frac{K_\alpha}{I_\alpha}}$	natural frequency in aerofoil-flap torsion
$\omega_\beta = \sqrt{\frac{K_\beta}{I_\beta}}$	natural frequency in flap torsion
$\omega_\delta = \sqrt{30 \frac{G}{pb^2}}$	natural frequency in camber
$\omega_h = \sqrt{\frac{K_h}{m}}$	natural frequency in plunge
$x_\alpha = \frac{S_\alpha}{mb}$	location of center of gravity of aerofoil-flap measured from a
$x_\beta = \frac{S_\beta}{mb}$	location of center of gravity of flap measured from c
α	angle of attack
β	aileron deflection
δ	camber
h	vertical displacement, plunge
$\kappa = \frac{\pi \rho b^2}{m}$	ratio of mass of a cylinder of air of diameter $2b$ to the mass of the aerofoil
ρ	aerofoil material density
ρ_∞	air density
$C(k)$	Theodorsen's wake function
ϕ_w	Wagner's indicial function

Subscripts

F	flutter
H	hinge moment component
L	lift component
Λ	bimoment component
M	moment component
a	aerodynamic term
qs	quasi-steady component
s	structural term

Contents

1	Introduction	7
1.1	Motivation and objectives	7
1.2	Literature review	8
1.3	Outline	9
2	Theory	10
2.1	Structural model	10
2.1.1	Aerofoil-flap system	10
2.1.2	Camber	12
2.2	Aerodynamic model	15
2.2.1	Theodorsen's theory	15
2.2.2	Indicial response method	17
2.3	Numerical algorithms	19
2.3.1	V-g method	20
2.3.2	Linear stability of state-space systems	21
2.3.3	Time-domain solution	21
3	Results and discussion	23
3.1	Analysis of flap effects	23
3.1.1	Validation	23
3.1.2	Parametric study	26
3.2	Analysis of camber effects	31
3.2.1	One degree of freedom	32
3.2.2	Two degrees of freedom	35
3.2.3	Three degrees of freedom	44
4	Conclusions	48
5	Further research	50
A	Theodorsen's geometric constants	55
B	Dynamics matrix	56
C	Validation of algorithms	58

1 Introduction

Aeroelasticity is the complex interaction among aerodynamic, elastic and inertia forces acting on a structure. Structures subject to an air-flow are not entirely rigid, so they deflect under aerodynamic forces. Meanwhile, the aerodynamic forces depend on the structural deformation, so a coupled problem arises: the equations of motion for both the structure and fluid must be solved simultaneously.

Flutter is the dynamic phenomena whereby the inertia forces can modify the behaviour of a flexible system so that energy is extracted from the incoming flow. The flutter or critical speed V_F and frequency ω_F are defined, respectively, as the lowest air-speed and the corresponding frequency at which a given structure would exhibit sustained, simple harmonic oscillations [8]. V_F represents the neutral stability boundary: oscillations are stable at speeds below it, but they become divergent above it.

The aeroelastic analysis and hence the flutter computation heavily relies on an accurate description of the unsteady aerodynamics. Unsteady flows arise for three reasons [9]: 1) the body is in unsteady motion (vibrating aerofoil), 2) the incident flow contains unsteady disturbances (gusts and turbulence) and 3) the body wake is unsteady (von Karman vortex street, for instance). The main feature of wakes is that they contain shear layers. These shear layers are usually unstable causing them to roll up into concentrated vortices and tending to imprint dominant frequencies of unsteady motion into the flow.

While the unsteady aerodynamic response of an aerofoil to a specific time history forcing can now be determined with considerable detail and accuracy using CFD, these solutions are complex and the required computational resources are extremely large [10]. This makes CFD methods impractical in routine aeroelastic analysis, and more approximate models must be used.

The classical simplified model of the aeroelastic system is the so-called typical section. It consists of a rigid plate of unit span with two degrees of freedom: rotation (pitch) and vertical translation (plunge). Typically, the structure is represented as a set of linear springs, and the aerodynamic forces are calculated using linear theory based on thin aerofoils. This is the approach taken in this project but two additional degrees of freedom will be considered: a trailing edge flap and chordwise deformations (camber).

1.1 Motivation and objectives

In recent years, the possible application of trailing edge flaps as a potential vibration and noise control measure has gained considerable attention within the helicopter and wind energy research areas [11], [12], [13], [14], [15], [16]. These flaps were typically rigid bodies,

but with recent breakthroughs in smart material actuator technology, it is possible to create actively controlled compliant trailing edge flaps [17], [18], [19].

On the other hand, different mechanisms that change airfoil camber have been proposed as an aerodynamically efficient substitute to discrete flap actuation to modify the aerodynamic forces [7]. Embedded piezoceramic actuators can be seen as the first generation of proposed morphing aerofoils.

The main objective of the project is to analyse these options and to determine their influence over the flutter boundaries of the typical aerofoil section:

1. The addition of a rigid flap to the classical pitch-and-plunge section has been widely studied in the bibliography. Concerning determination of stability boundaries, where the project focuses on, the problem has been solved and extensively reported. Hence, in this case, the work has been primarily aimed at validation. Numerical algorithms have been coded and results compared to published figures. This validation step is a necessary previous step for the second goal.
2. The introduction of the camber degree of freedom in the context of flutter computation represents a novelty. Therefore, the work has been more oriented toward understanding the physical phenomena. It has been tried to identify mechanisms that drive flutter and determine their origin.

1.2 Literature review

In the 30's, Theodorsen and Garrick published critical advances in the study of the unsteady air loads on an oscillating aerofoil (in chronological order, references [20], [21], [1], [2], [22] and [23]). They were the first ones to obtain a closed-form solution to the problem. This approach assumed harmonic oscillations in inviscid and incompressible flow subject to small disturbances. The most important developments, including the incorporation of an oscillating trailing edge flap, were presented in [1] and extended to include the effect of aerodynamic balance and the effect of a tab added to the flap in [22].

Theodorsen's theory has been widely used despite its strong assumption of simple harmonic motion. This assumption makes the theory to be valid, strictly, only at the flutter boundary. Another significant limitation of Theodorsen's approach is that the solution method is limited to the frequency domain. This can be overcome by using a indicial response method, as proposed by Wagner [24] before Theodorsen published his theory. Wagner's theory also assumes incompressible potential flow and it can be proved, that, in fact, Theodorsen's and Wagner's theory are equivalent, representing a Fourier transform pair [25].

A practical way to tackle the indicial response method is a state-space formulation in the

time-domain, as proposed, for instance, by Leishman and Nguyen in [10]. Following this approach, Leishman [26] and Hariharan and Leishman [27] described the development of an unsteady aerodynamic theory for the effects of a trailing edge flap.

Chordwise deformations were already introduced by Spielberg [4] in 1953, assuming a parabolic bending of the profile and following Theodorsen's unsteady liner aerodynamic theory. Rodden [5], in 1969, based on Spielberg's approach, formulated the flutter problem and proposed how to solve it by means of which represents a forerunner of the current V-g method. More recently (2008), Palacios and Cesnik [7] presented their independently developed model for camber. Their definition of the new degree of freedom differs from the previous, but both theories are equivalent. On the other hand, in the wind energy environment, Gaunaa [6] in 2006 also studied the unsteady 2D force distribution on a variable geometry aerofoil undergoing arbitrary motion, under the assumption of incompressible, irrotational and inviscid flow.

Regarding solution methods for the equations of motion, Theodorsen himself proposed how to compute the flutter onset from the equations he derived in the frequency domain. Already in [1] he presented a way to proceed, but in subsequent papers he suggested improved methods. After some manipulation, he achieved the simplest procedure in [23]. All procedures involved the same limitation: the last step was carried out graphically with the consequent lack of accuracy. Besides, Theodorsen's procedure is not general and it is dependent on the degrees of freedom considered. Currently, much more advanced computational algorithms exist to solve the flutter problem [28], and these will be implemented here.

1.3 Outline

The required theoretical concepts are briefly explained in section 2. This concerns the structural and aerodynamic models, as well as the numerical algorithms to solve the aeroelastic equations of motion. Section 3 presents and discusses flutter results for the two different aeroelastic systems that have been analysed: aerofoil-flap and aerofoil-camber. The effects of both are described. The main conclusions of the work are summarized in section 4 and finally, improvement ideas and further research are proposed in section 5.

2 Theory

The objective of this section is the introduction of the unsteady aeroelastic equations of motion and the numerical algorithms to solve them. These equations govern the behaviour of the system subject to study and enable the analysis of different aspects, such as time-evolution or stability.

In this case, the general system subject to study is an aerofoil consisting of four degrees of freedom: pitch, plunge, flap deflection and camber. However, in principle, flap deflection and camber will not appear together in practical applications, since their purpose is the same. Consequently, simplified combinations of three degrees of freedom will be studied, namely pitch-plunge-flap and pitch-plunge-camber.

The aeroelastic equations comprise structural terms and aerodynamic loads, which are introduced in the next sections. No derivation of equations will be presented here and the reader is encouraged to consult the relevant references for further details. In the last section numerical algorithms are introduced, primarily focused on flutter computation.

2.1 Structural model

The structural model is different for the pitch-plunge-flap and pitch-plunge-camber systems, so it is presented in separate sections. The aerofoil-flap combination has been widely studied and it is presented first in 2.1.1. The inclusion of the camber degree of freedom in this context is a relative novelty and it is therefore studied next in 2.1.2.

Both models are linear and do not account for structural damping. According to [23], the influence of structural damping on flutter calculations is critical. However, there are several reasons not to include it: first of all, the objective of this study focuses on the unsteady aerodynamics; secondly, it is relatively difficult to obtain realistic physical values of damping coefficients and finally and above all, neglecting structural damping means that flutter results are on the safety side.

2.1.1 Aerofoil-flap system

Figure 1 shows the typical section of an aerofoil-flap combination without camber. The nomenclature follows that of [1]. It has three degrees of freedom, namely pitch, plunge and flap deflection. The pitch, denoted by α , is positive nose-up; the plunge h is positive downwards and the flap deflection β , positive down. The midchord length is denoted by b , which is used as reference length. The elastic axis is located at a distance a from the midchord and the distance to the hinge is measured by c . The center of gravity of

the aerofoil-flap combination is located at a distance x_α from the elastic axis whereas the position of the center of mass of the flap is referred to the hinge, and given by x_β .

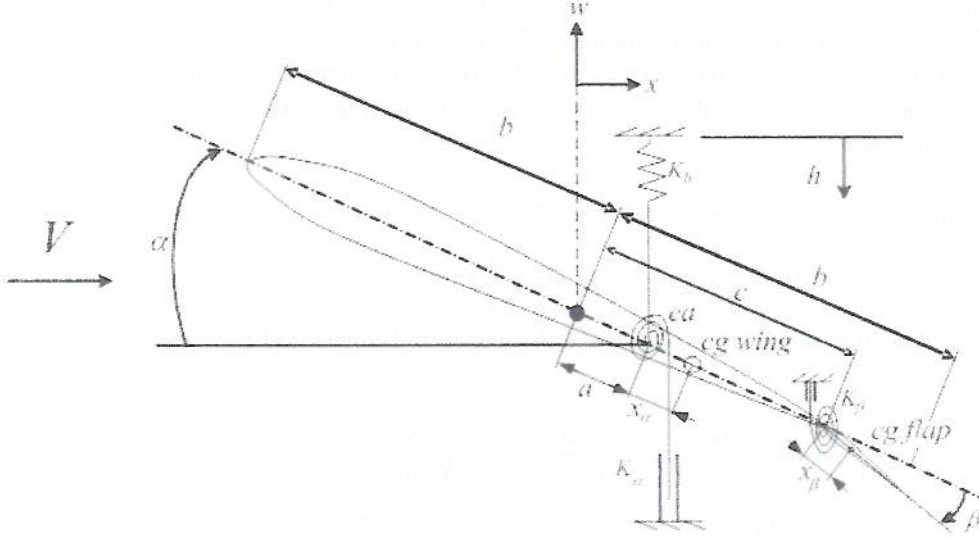


Figure 1: Aerofoil-flap combination with 3 degrees of freedom

Note that in figure 1 α and β represent the sum of rigid and elastic deflections:

$$r = r_0 + \bar{r} \quad (1)$$

where r can be α or β . r_0 represents the deflections set up by the pilot whereas \bar{r} corresponds to the elastic deformations due to the compliances within the system. Only the elastic deformations contribute to the energy of the system. For the sake of simplicity, it will be assumed that the rigid deformations are zero, which does not affect the results for being the problem linear. Hence, subsequently $r = \bar{r}$.

The vertical displacement of the aerofoil as a function of the coordinate x is given by

$$w = -h - \alpha(x - a) - H(x - c)\beta(x - c) \quad (2)$$

where $H(x - c)$ represents the Heaviside function:

$$H(x - c) = \begin{cases} 0, & x < c \\ 1, & x > c \end{cases} \quad (3)$$

The corresponding kinetic energy per unit length is

$$T = \int_{-b}^b \frac{1}{2} \rho t_p \dot{w}^2 dx = \frac{1}{2} m \dot{h}^2 + \frac{1}{2} I_\alpha \dot{\alpha}^2 + \frac{1}{2} I_\beta \dot{\beta}^2 + S_\alpha \dot{\alpha} \dot{\beta} + S_\beta \dot{\beta} \dot{h} \quad (4)$$

Here ρ represents the density of the material, t_p the thickness of the aerofoil and m the mass; S_α and S_β correspond to the static moments of the aerofoil-flap and flap respectively, the former referred to a and the latter to c ; I_α and I_β are the moments of inertia and K_α , K_β and K_h stand for the relevant stiffnesses, represented by springs. All these quantities are expressed per unit span.

On the other hand, the strain energy per unit length is given by

$$U = \frac{1}{2} K_\alpha \alpha^2 + \frac{1}{2} K_\beta \beta^2 + \frac{1}{2} K_h h^2 \quad (5)$$

Using Lagrange's principle and introducing the following non-dimensional parameters,

$$\begin{aligned} \omega_\alpha &= \sqrt{\frac{K_\alpha}{I_\alpha}}, \omega_\beta = \sqrt{\frac{K_\beta}{I_\beta}}, \omega_h = \sqrt{\frac{K_h}{m}} \\ r_\alpha &= \sqrt{\frac{I_\alpha}{mb^2}}, r_\beta = \sqrt{\frac{I_\beta}{mb^2}}, x_\alpha = \frac{S_\alpha}{mb}, x_\beta = \frac{S_\beta}{mb} \\ \kappa &= \frac{\pi \rho b^2}{m} = \frac{1}{\mu} \end{aligned} \quad (6)$$

the aeroelastic equations of motion of the pitch-plunge-flap system, in the absence of external forces other than aerodynamic loads, are

$$r_\alpha^2 \ddot{\alpha} + [r_\beta^2 + (c - a)x_\beta] \ddot{\beta} + x_\alpha \frac{\ddot{h}}{b} + \omega_\alpha^2 r_\alpha^2 \alpha = 2 \frac{\kappa}{\pi} \left(\frac{V}{b} \right)^2 C_M(t) \quad (7)$$

$$[r_\beta^2 + (c - a)x_\beta] \ddot{\alpha} + r_\beta^2 \ddot{\beta} + x_\beta \frac{\ddot{h}}{b} + \omega_\beta^2 r_\beta^2 \beta = 2 \frac{\kappa}{\pi} \left(\frac{V}{b} \right)^2 C_H(t) \quad (8)$$

$$x_\alpha \ddot{\alpha} + x_\beta \ddot{\beta} + \frac{\ddot{h}}{b} + \omega_h^2 \frac{h}{b} = \frac{\kappa}{\pi} \left(\frac{V}{b} \right)^2 C_L(t) \quad (9)$$

where C_M , C_H and C_L represent the coefficients of the corresponding aerodynamic loads: pitching moment, hinge moment and lift.

2.1.2 Camber

Typically, low-order aeroelastic analyses assume that the cross sections are rigid but there are situations in which this assumption cannot be justified [7]. As a result, in order to

account for chordwise deformations, the camber degree of freedom is included.

Flexibility and hence deformations will be limited to a change of camber and the model proposed by Palacios and Cesnik [7] will be used. It assumes small deformations and thin-aerofoil theory. Henceforth, this model will be deemed to represent adequately the physics of the problem.

Figure 2 illustrates this model, which entails three degrees of freedom: pitch (α), plunge (h) and camber deformation (δ).

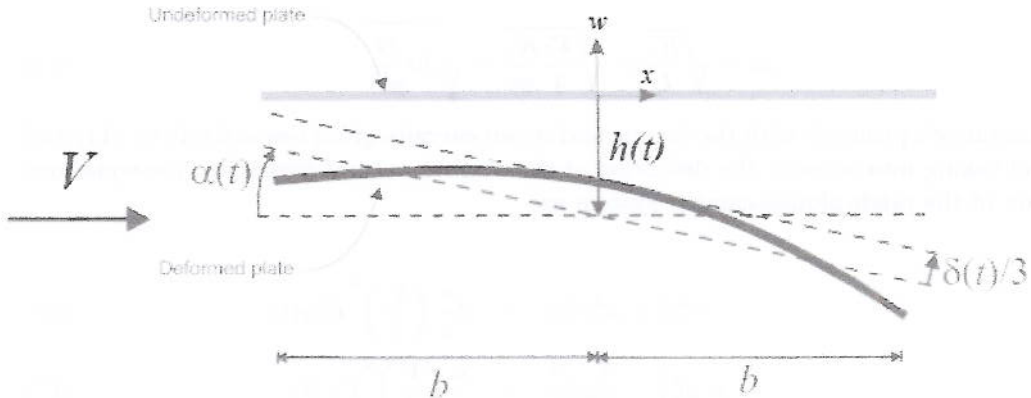


Figure 2: Thin-plate with camber deformation

The variation of camber is defined by a single parabolic mode, which requires the area centroid of the section to remain unaltered; i.e., both the elastic axis and the center of gravity of the section are located at the midchord. This implies that the cross-sectional inertia contributions become uncoupled, since the vertical displacement is given by

$$w = -h - \alpha x - \left[\left(\frac{x}{b} \right)^2 - \frac{1}{3} \right] \delta \quad (10)$$

leading to the kinetic energy per unit length being

$$T = \int_{-b}^b \frac{1}{2} \rho t_p \dot{w}^2 dx = \frac{1}{2} m \dot{h}^2 + \frac{1}{6} m b^2 \dot{\alpha}^2 + \frac{2}{45} m \dot{\delta}^2 \quad (11)$$

In this case, the strain energy per unit length is

$$U = \frac{1}{2} K_\alpha \alpha^2 + \frac{1}{2} K_h \left(h - \frac{\delta}{3} \right)^2 + \frac{1}{2} K_\delta \delta^2 \quad (12)$$

Note the link between plunge and camber, which will lead to coupling stiffness terms in the equations of motion. From the structural model [7], the camber stiffness is given by

$$K_\delta = \frac{16Gt_p}{3b} \quad (13)$$

where G is the shear modulus of the material. The camber moment of inertia can be defined as

$$I_\delta = \frac{4}{45}m \quad (14)$$

and thus, the camber natural frequency would in turn be

$$\omega_\delta = \sqrt{\frac{K_\delta}{I_\delta}} = \sqrt{\frac{45}{4} \frac{K_\delta}{m}} = \sqrt{30 \frac{G}{\rho b^2}} \quad (15)$$

Using Lagrange's principle with the kinetic and strain energies given respectively by (11) and (12), and taking into account the definition of the camber natural frequency, the equations of motion of the pitch-plunge-camber system are

$$r_\alpha^2 \ddot{\alpha} + \omega_\alpha^2 r_\alpha^2 \alpha = 2 \frac{\kappa}{\pi} \left(\frac{V}{b} \right)^2 C_M(t) \quad (16)$$

$$\frac{\ddot{h}}{b} + \omega_h^2 \frac{h}{b} - \frac{1}{3} \omega_h^2 \frac{\delta}{b} = \frac{\kappa}{\pi} \left(\frac{V}{b} \right)^2 C_L(t) \quad (17)$$

$$\frac{\ddot{\delta}}{b} - \frac{1}{3} \omega_h^2 \frac{h}{b} + \left(\frac{5}{4} \omega_h^2 + \omega_\delta^2 \right) \frac{\delta}{b} = \frac{45}{4} \frac{\kappa}{\pi} \left(\frac{V}{b} \right)^2 C_\Lambda(t) \quad (18)$$

where Λ represents the aerodynamic load corresponding to the camber bimoment, which has dimensions of force per unit length.

The sets of equations of motion (7-9) and (16-18) can also be expressed in abridged form as

$$M_s \ddot{\mathbf{r}} + K_s \mathbf{r} = \mathbf{F} \quad (19)$$

where $\mathbf{r} = [\alpha \ \beta \ h]^T$ or $\mathbf{r} = [\alpha \ h \ \delta]^T$ are the degrees of freedom of the system, M_s and K_s are the mass and stiffness structural matrices respectively and $\mathbf{F} = [F_1 \ F_2 \ F_3]^T$ represents the aerodynamic forcing.

2.2 Aerodynamic model

The equations of motion of the aerofoil-flap and aerofoil with camber have been introduced in section 2.1. However, only the structural terms have been explicitly presented and the aerodynamic loads have not been expanded. These loads are obtained from linear unsteady aerodynamics theory.

Theodorsen was the first to obtain a closed-form solution to the unsteady aerodynamic loads over an aerofoil, but the solution method is limited to the frequency domain. In order to attain a time-domain solution, the indicial response method proposed by Wagner [24] can be used. Both approaches are presented here.

2.2.1 Theodorsen's theory

Theodorsen's approach assumed small harmonic oscillations of an inviscid and incompressible flow. Unsteady potential theory was used to calculate the velocity potentials due to the flow around an oscillating flat plate, oscillating flap or a combination of both [1]. The expressions for the velocity potentials were computed based on the transformation of an aerofoil into a circle, previously obtained in [20] and [21]. From these velocity potentials, the local pressures were obtained, and by integration the forces and moments acting on the aerofoil and flap. For convenience the response of the forces were split into non-circulatory (apparent mass) and circulatory parts.

Theodorsen provided the aerodynamic coefficients corresponding to pitch, plunge and flap in [1], but he did not include chordwise deformations. The expression for the camber bimoment can be obtained from different sources, such as [4], [5] or [7]. Here the camber degree of freedom defined by Palacios and Cesnik [7] has been used (refer to figure 2).

The aerodynamic loads are thus given by

$$\begin{aligned}
 C_M = & -\frac{1}{2} \left[(T_4 + T_{10}) \beta + \frac{\pi}{b} \delta \right] \\
 & -\frac{1}{2V} \left\{ \pi \left(\frac{1}{2} - a \right) b \dot{\alpha} + \left[T_1 - T_8 - (c - a) T_4 + \frac{1}{2} T_{11} \right] b \dot{\beta} + \frac{\pi}{2} \dot{\delta} \right\} \\
 & + \frac{1}{2V^2} \left\{ -\pi \left(\frac{1}{8} + a^2 \right) b^2 \ddot{\alpha} + [T_7 + (c - a) T_1] b^2 \ddot{\beta} + \pi a b \ddot{h} \right\} \\
 & + \pi \left(a + \frac{1}{2} \right) C(k) [\alpha_{qs} + \beta_{qs} + \delta_{qs}]
 \end{aligned} \tag{20}$$

$$\begin{aligned}
C_H &= \frac{1}{2} \frac{T_4 T_{10} - T_5}{\pi} \beta \\
&\quad + \frac{1}{2V} \left\{ \left[2T_9 + T_1 - T_4 \left(a - \frac{1}{2} \right) \right] b\dot{\alpha} + \frac{T_4 T_{11}}{2\pi} b\dot{\beta} \right\} \\
&\quad + \frac{1}{2V^2} \left(-2T_{13}b^2\ddot{\alpha} + \frac{T_3}{\pi} b^2\ddot{\beta} - T_1 b\ddot{h} \right) \\
&\quad - \frac{1}{2} T_{12} C(k) [\alpha_{qs} + \beta_{qs} + \delta_{qs}] \tag{21}
\end{aligned}$$

$$\begin{aligned}
C_L &= \frac{1}{V} \left(-\pi b\dot{\alpha} + T_4 b\dot{\beta} \right) \\
&\quad + \frac{1}{V^2} \left(\pi ab^2\ddot{\alpha} + b^2 T_1 \ddot{\beta} - \pi b\ddot{h} \right) \\
&\quad - 2\pi C(k) [\alpha_{qs} + \beta_{qs} + \delta_{qs}] \tag{22}
\end{aligned}$$

$$\begin{aligned}
C_A &= \frac{\pi}{2b} \delta + \frac{1}{V} \frac{b}{3} \dot{\alpha} + \frac{1}{V^2} \left(\frac{b}{12} \ddot{h} - \frac{b}{36} \ddot{\delta} \right) \\
&\quad - \frac{\pi}{3} C(k) [\alpha_{qs} + \beta_{qs} + \delta_{qs}] \tag{23}
\end{aligned}$$

where T_i are geometric constants, with a fixed value for a given cross-section. They arise from the integration of velocity potentials in the derivation of the aerodynamic loads. They only depend on a and c : $T_i = T_i(a, c)$. The exact expressions to compute them is enclosed in appendix A.

For the aerofoil-flap system (section 2.1.1) equation (23) must be ignored, as well as dependencies with respect to δ in the rest of equations. In contrast, if camber is considered (section 2.1.2), equation (21) and β are unnecessary. Recall also that in this case the structural model requires $a = 0$.

The symbols α_{qs} , β_{qs} and δ_{qs} denote the quasi-steady angle of attack, flap deflection and camber deformation respectively and they are given by

$$\alpha_{qs} = \alpha + \frac{b}{V} \left(\frac{1}{2} - a \right) \dot{\alpha} + \frac{\dot{h}}{V} \tag{24}$$

$$\beta_{qs} = \frac{T_{10}}{\pi} \beta + \frac{b T_{11}}{2\pi V} \dot{\beta} \tag{25}$$

$$\delta_{qs} = \frac{\delta}{b} + \frac{\dot{\delta}}{6V} \tag{26}$$

The circulatory contribution in equations (20-23) corresponds to the terms multiplying $C(k)$, known as Theodorsen's function (see [1] for details). This complex function accounts

for the effects of the shed wake on the unsteady air loads and depends only on the so-called reduced frequency k , given by

$$k = \frac{\omega b}{V} \quad (27)$$

The rest of the terms in equations (20-23) are called non-circulatory or apparent mass.

2.2.2 Indicial response method

Theodorsen's theory (as described in section 2.2.1) is formulated in the frequency domain, as a function of the parameter k , which is implicit in the solution since it depends on the frequency of oscillation. However, a theory formulated in the time domain is more generally applicable [29]. For incompressible flow, Wagner [24] obtained a solution for the indicial lift on a thin aerofoil undergoing a step change in angle of attack.

By definition, an indicial function is the response to a step change in a set of defined parameters, such as a step change in angle of attack, flap deflection, pitch rate, flap rate or a penetrating gust field. If the indicial response to a step change is known, then the unsteady loads to an arbitrary input can be obtained through the superposition of indicial aerodynamic responses using the so-called Duhamel's integral.

Assuming two-dimensional incompressible potential flow over a thin aerofoil, the circulatory terms in equations (20-23) can be written as [25]

$$C(k) r_{qs} = r_{qs}(0)\phi_w(s) + \int_0^s \frac{dr_{qs}}{d\tau} \phi_w(s - \tau) d\tau \quad (28)$$

where s is the non-dimensional time, given by

$$s = \frac{Vt}{b} \quad (29)$$

ϕ_w is Wagner's function, which, as Theodorsen's function $C(k)$, accounts for the influence of the shed wake. In fact, both Wagner's and Theodorsen's functions represent a Fourier transform pair. Wagner's function is known exactly in terms of Bessel functions (see [8] for details), but for practical implementation it is useful to represent it approximately. One of the most useful expressions is an exponential of the form

$$\phi_w(s) \approx 1 - A_1 e^{-b_1 s} - A_2 e^{-b_2 s} \quad (30)$$

Several fits of acceptable accuracy have been proposed [25]:

	A_1	A_2	b_1	b_2
Leishman [26]	0.2048	0.2952	0.057	0.333
R. T. Jones [30]	0.165	0.335	0.0455	0.3
W. P. Jones [31]	0.165	0.335	0.041	0.32

Table 1: Different exponential approximations for the Wagner function

The exponential approximation has the advantage of a simple Laplace transform, which is crucial in the steps to follow. Equation (28) is usually solved numerically for discrete values of non-dimensional time s . Using the exponential approximation of Wagner's function (30), there are several ways to tackle the calculation of the circulatory aerodynamic loads. The state-space formulation is presented here, which is suitable for frequency- and time-domain solution methods.

State-space formulation The state is the collection of variables that completely characterizes a system at present and permits the prediction of its future behaviour [32]; for given inputs to a system, as long as the states are known, the outputs can be determined. A linear system can be represented in its state-space form as follows

$$\dot{\mathbf{x}} = A\mathbf{x} + Bu \quad (31)$$

$$\mathbf{y} = C\mathbf{x} + Du \quad (32)$$

where \mathbf{x} , \mathbf{u} and \mathbf{y} are the state, input and output vectors respectively.

The state-space equations describing the unsteady aerodynamics of the aerofoil-flap system can be obtained by direct application of Laplace transforms to the indicial response, as explained in [10]. From the Laplace transform of the corresponding impulse response, the transfer function is obtained. From this transfer function, the aerodynamic response can be written in state-space form following [26]. It can be expressed in controllable canonical form as

$$\begin{bmatrix} \dot{z}_i \\ \dot{z}_{i+1} \end{bmatrix} = \begin{bmatrix} 0 & 1 \\ -b_1 b_2 \left(\frac{V}{b}\right)^2 & -(b_1 + b_2) \frac{V}{b} \end{bmatrix} \begin{bmatrix} z_i \\ z_{i+1} \end{bmatrix} + \begin{bmatrix} 0 \\ 1 \end{bmatrix} r_{qs} \quad (33)$$

with the outputs

$$C(k) r_{qs} = \left[\frac{b_1 b_2}{2} \left(\frac{V}{b}\right)^2 (A_1 b_1 + A_2 b_2) \left(\frac{V}{b}\right) \right] \begin{bmatrix} z_i \\ z_{i+1} \end{bmatrix} + \frac{1}{2} r_{qs} \quad (34)$$

The output given by (34) corresponds to the circulatory terms of the aerodynamic loads of equations (20-23). The new aerodynamic states are denoted by z_i , with $i = 1$ corresponding to $r_{qs} = \alpha_{qs}$, $i = 3$ to $r_{qs} = \beta_{qs}$ and $i = 5$ to $r_{qs} = \delta_{qs}$. Depending on which system is to be studied, β_{qs} or δ_{qs} and the respective aerodynamic states will be ignored.

The main benefit of state-space formulation is that the equations can be appended to the equations of motion directly, very useful in aeroservoelastic analysis. Furthermore, it permits a straightforward addition of more features to the model, such as gust response and compressibility.

Defining the states

$$\mathbf{x} = [\alpha \ \beta \ h \ \delta \ \dot{\alpha} \ \dot{\beta} \ \dot{h} \ \dot{\delta} \ z_1 \ z_2 \ z_3 \ z_4 \ z_5 \ z_6]^T \quad (35)$$

and after some manipulation, the equations of motion (19) can be reformulated as in equation (31), where dynamics matrix A is given in appendix B.

2.3 Numerical algorithms

From a practical point of view, the flutter onset is one of the most important aspects in aeroelasticity. Depending on the form of the equations used, the computation of the flutter boundaries can be undertaken in different ways. However, the foundation of these methods lay on the two principal theories presented before: Theodorsen's theory (section 2.2.1) and indicial approach (section 2.2.2).

Theodorsen himself proposed several ways to compute flutter onset, but all of them are graphical and they are not general for any number of degrees of freedom. Current computer resources offer the advantage of solving the problem numerically and benefiting from modern procedures to tackle the flutter problem. These techniques are more efficient, accurate and easier to implement.

If Theodorsen's theory is considered for the description of the aerodynamic loads, there are several engineering solutions to the flutter problem used in industry, such as the V-g method (section 2.3.1). If, otherwise, indicial approach and state-space formulation are used, determination of flutter reduces to the stability analysis of a linear state-space model (section 2.3.2). Finally, the flutter computation can also be carried out in the time domain (section 2.3.3).

The first two techniques (V-g and linear analysis of linear state-space system) are performed in the frequency-domain. They are far more efficient for flutter calculations, but can only

be applied in the linear regime and time-domain solution procedures are required for non-linear analysis. Although inefficient for linear flutter analysis, solving the problem in the time-domain allows to validate the algorithm, which would be very useful if a non-linear analysis was to be undertaken.

2.3.1 V-g method

The V-g method is based on the introduction of an unknown fictitious structural damping (g), proportional to the generalized stiffness matrix, in phase with the velocity and independent of the frequency [28]. Introducing the expressions given by Theodorsen for the aerodynamic loads (section 2.2.1) and after some manipulation, the modal flutter equation is obtained

$$\left[\omega M_s + (1 + ig)K_s - \frac{2q_\infty}{\rho} A(k) \right] \bar{r} = 0 \quad (36)$$

where subscripts s implies structural matrices, \bar{r} represent the amplitudes of the generalized coordinates or degrees of freedom and $A(k)$ is the complex matrix of aerodynamic coefficients. From the combinations of dynamic pressure q_∞ and oscillation frequency ω for which $g = 0$, the one that corresponds to the smallest positive value of dynamic pressure determines the flutter onset point.

Manipulation of (36) yields

$$\left\{ K_s^{-1} \left[M_s + \left(\frac{b}{k} \right)^2 A(k) \right] - \Omega I \right\} \bar{r} = 0 \quad (37)$$

where

$$\Omega = \frac{1 + ig}{\omega^2} \quad (38)$$

Equation (37) defines an eigenvalue problem at each reduced frequency. The flutter point will be found when an eigenvalue has zero imaginary part, since in such case $g = 0$. If there are more than one point with $Im(\Omega) = 0$, the flutter conditions will be determined by the eigenvalue with the smaller speed.

Apart from the flutter speed, the V-g method provides very useful information to interpret the flutter mechanism. Results are usually plotted as V-g and V- ω graphs. The flutter speed can be clearly identified in the V-g plot, but it can also be guessed in some cases from the V- ω , when flutter is due to mode interaction. In this cases, there is a frequencies coalescence. This enables to determine which modes are interchanging energy and are, therefore, responsible for flutter. The eigenvectors of the system can be used to further

confirm this. This will be seen more clearly with results in section 3.

As it is based on Theodorsen's exact analytic theory, the only approximation of the V-g method lies in the numerical computation. Nevertheless, results are only valid at flutter point ($g = 0$) and they can be difficult to interpret or even misleading [33].

2.3.2 Linear stability of state-space systems

Indicial approach and state-space formulation (2.2.2) lead to a dynamics matrix that governs the behaviour of the system and enables future prediction. The analysis of flutter in this case is straightforward and it can be performed in the frequency domain, since the eigenvalues of the dynamics matrix A determine directly the stability of the system.

If for a given velocity any of the eigenvalues has zero real part, the system is neutrally stable, i.e., it defines the flutter onset.

In this procedure Wagner's function is not represented exactly, but it is the fastest and highly accurate.

2.3.3 Time-domain solution

The procedures explained so far only work in the linear regime. If non-linear aerodynamics, such as dynamic stall, were to be considered only a time-domain solution method would be applicable.

For harmonic motion, the temporal evolution of the oscillation of the degrees of freedom can be expressed as

$$\alpha = \alpha_0 e^{\sigma_\alpha t} \cos(\omega t) \quad (39)$$

$$\beta = \beta_0 e^{\sigma_\beta t} \cos(\omega t + \varphi_\beta) \quad (40)$$

$$h = h_0 e^{\sigma_h t} \cos(\omega t + \varphi_h) \quad (41)$$

$$\delta = \delta_0 e^{\sigma_\delta t} \cos(\omega t + \varphi_\delta) \quad (42)$$

The sign of the exponent of these expressions will determine whether the system is stable or not. If any σ is positive, the oscillations will grow in time and thus the system is unstable. In contrast, a negative value implies decaying amplitude, so the oscillation is damped out, as illustrated in figure 3. The value of σ depends on the velocity; therefore, the smallest value of velocity that makes $\sigma = 0$ is the flutter speed.

This method is computationally very expensive compared to the procedures presented before, since, to compute the value of σ the time history must be obtained for each value of

velocity. To obtain an acceptable accuracy, a long enough period of time must be considered and moreover, this period is longer the closest to zero σ is.

Depending on the form of the equations, there are different techniques to solve the set of equations in the time domain, such as Newmark- β and Runge-Kutta.

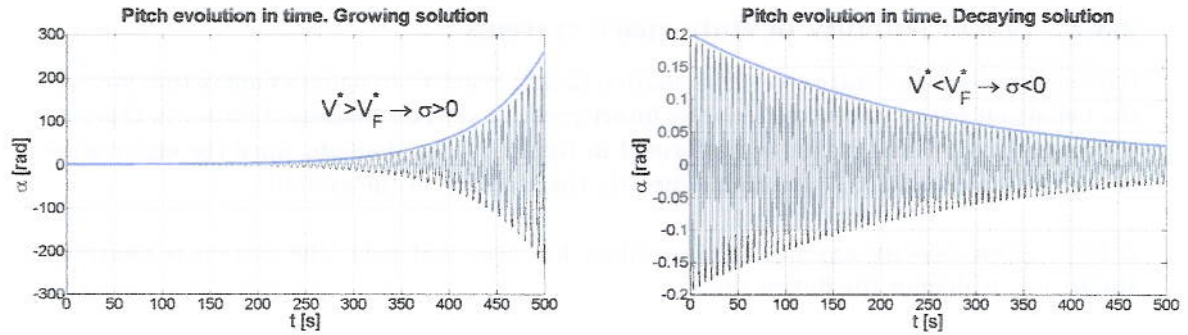


Figure 3: Temporal evolution of pitch. Stable and unstable solutions

3 Results and discussion

This section presents the results obtained as the afore-explained theory is applied. The influence of flap and camber over the typical aerofoil is investigated separately. The analysis is focused on flutter computation for both cases, but the objectives pursued in each case are different.

3.1 Analysis of flap effects

In this section only pitch, plunge and flap degrees of freedom are considered. Hence, the relevant equations of motion are (7-9) and dependence on camber δ is removed in the aerodynamic loads. For this system, the set of parameters that univocally determines the flutter problem is

$$a, c, x_\alpha, r_\alpha, x_\beta, r_\beta, \frac{\omega_h}{\omega_\alpha}, \frac{\omega_\beta}{\omega_\alpha}, \kappa \quad (43)$$

The first objective of this section has been the validation of the coded algorithms, since numerous published results are available. V-g, state-space linear stability and time-domain procedures have been implemented in Matlab® and the results have been compared to published figures. Secondly, a parametric study has been undertaken to analyse the role played by different parameters of the structural model introduced in section 2.1.1.

3.1.1 Validation

The validation of the implementation has been carried out in two steps. First, frequency-domain methods are tested (V-g and linear state-space) against [1]. After they are checked, the time-domain procedure is validated.

Frequency domain Results are compared to figures by Theodorsen in [23]. For the state-space formulation, coefficients proposed by Leishman (refer to table 1) are considered. Graphs for varied combinations of the parameters listed above (43) are enclosed in appendix C, figures 37-44. In all of them, non-dimensional flutter speeds ($V_F^* = \frac{V_F}{b\omega_\alpha}$) are presented as a function of the frequency ratio $\omega_\beta/\omega_\alpha$; values of the parameters are included in the caption. Theodorsen presented an amazing amount of data, so here a selection has been done.

As can be seen, both methods provide fair agreement with published data in some cases, but the discrepancy is significant in others. Although the trends are always nicely captured, the errors in some cases are beyond expected. V-g and Leishman's state-space methods exhibit an excellent agreement between them, so either of them will be considered henceforth.

Theodorsen and Garrick solved graphically the equations of motion. In order to check possible reasons for the inconsistency with respect to the published values, these equations have been solved numerically. Every step has been validated against the example published in [2] and only the last step has been performed numerically. Figure 4 shows the results:

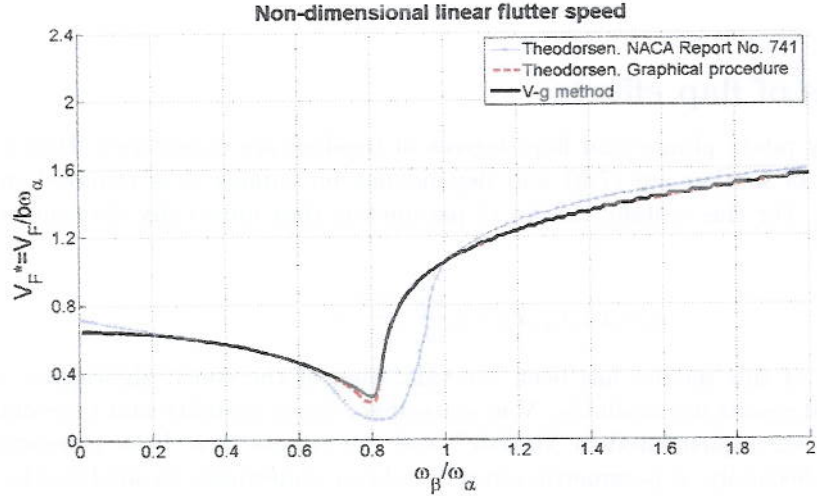


Figure 4: V-g method and Theodorsen's graphical procedure against results by Theodorsen and Garrick [23]. $a = -0.2$, $c = 0.6$, $\kappa = 0.2$, $x_\alpha = 0$, $r_\alpha^2 = 1$, $x_\beta = 0$, $r_\beta^2 = 0.002$, $\frac{\omega_h}{\omega_\alpha} = 0.607$

The new approach manifests a much better agreement with the V-g method than with the published data. These inconsistencies evidence mistakes in the published plots, as was already reported by Zeiler [3]. Although limited to 2 degrees of freedom, Zeiler's study implies that a number of plots in [23] are erroneous. Considering the evolution of numerical computations and the time spent checking the derivations, he confidently states that Theodorsen and Garrick made some mistakes in the computation of the flutter boundaries.

Figure 5 shows some results obtained by Zeiler, compared to figures obtained by Theodorsen and Garrick [23] and the V-g method. As can be observed, the agreement with Zeiler is very good, whereas Theodorsen's results deviate considerably. This confirms the validity of Zeiler's statement and provides evidence of the validity of the results obtained here.

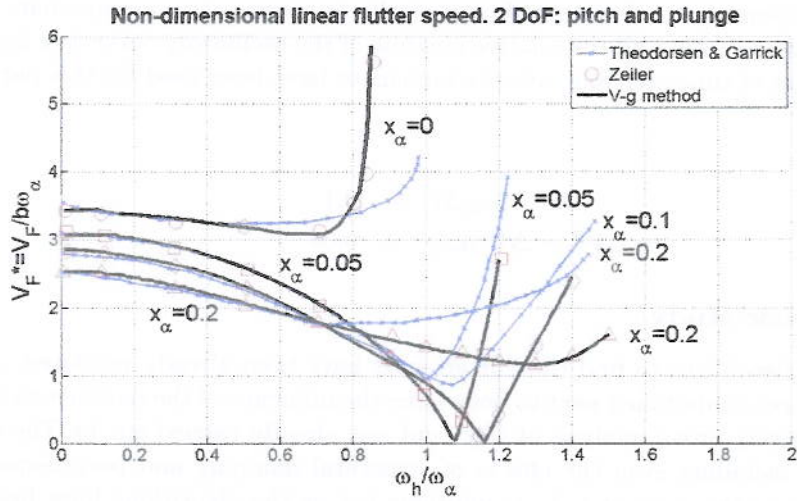


Figure 5: Comparison for a two-degrees of freedom system. V-g, Zeiler [3] and Theodorsen and Garrick [23]. $a = -0.3$, $\kappa = 0.05$, $r_\alpha^2 = 0.25$

Time-domain Figure 6 shows the results obtained applying the time-domain solution, using a fourth order Runge-Kutta method. The agreement with V-g is remarkable.

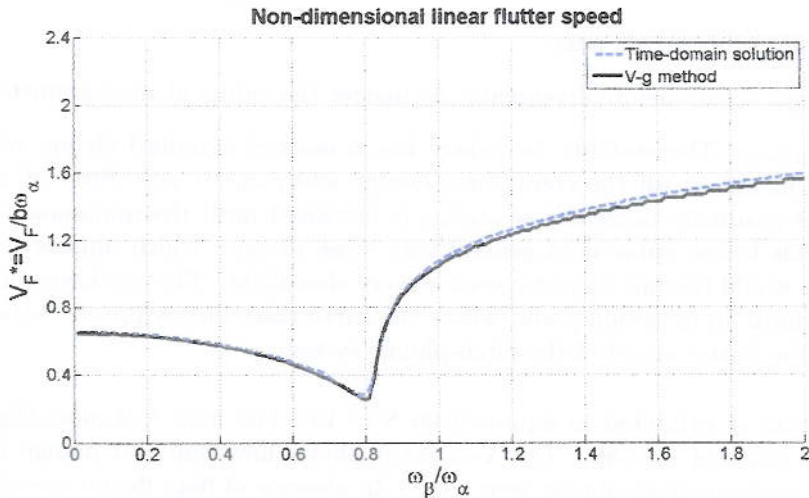


Figure 6: Non-dimensional flutter speed $V_F^* = \frac{V_F}{b\omega_\alpha}$ as a function of the frequency ratio $\omega_\beta/\omega_\alpha$. $a = -0.2$, $c = 0.6$, $\kappa = 0.2$, $x_\alpha = 0$, $r_\alpha^2 = 1$, $x_\beta = 0$, $r_\beta^2 = 0.002$, $\frac{\omega_h}{\omega_\alpha} = 0.607$

The value of the exponent σ is determined numerically by means of an approximate fitting procedure, taking into account all the relative maxima of the oscillatory curve (see figure 3). The following values of time-step and velocity increment have been used for this particular simulation:

$$\begin{aligned}\Delta t^* &= \omega_\alpha \Delta t = 0.1 \\ \Delta V^* &= \Delta V / b\omega_\alpha = 0.01\end{aligned}$$

3.1.2 Parametric study

As the numerical algorithms to find the flutter onset have been already validated, a parametric study has been undertaken next to determine the influence of the parameters (43) on this value. A relatively broad analysis of this kind was already carried out by Theodorsen and Garrick [23], including even the effects of structural damping and partial-span flap. The range covered in this project is less ambitious but as the algorithms have been validated, the results should be deemed to be more reliable. Again, non-dimensional flutter speed (V_F^*) is presented as a function of the frequency ratio $\omega_\beta/\omega_\alpha$. The other 8 parameters that univocally define the problem (43) are varied to see their influence. The following combination of values is used as reference, which are based on [23]:

$$a = -0.2, c = 0.6, x_\alpha = 0.2, r_\alpha^2 = 1, x_\beta = 0.002, r_\beta^2 = 0.002, \frac{\omega_h}{\omega_\alpha} = 0.607, \kappa = 0.2 \quad (44)$$

The main results are summarized next:

- Flutter always occurs before divergence, no matter the values of the parameters.
- *Effect of $\omega_\beta/\omega_\alpha$.* The stability boundary has a marked standard shape, which is maintained in almost all the conditions, except when $\omega_h \rightarrow \omega_\alpha$. First of all, the flutter onset gradually decreases as $\omega_\beta/\omega_\alpha$ is increased until the minimum value is reached. This lowest value is in general very close to zero, which implies that the aerofoil-flap would become unstable even at very slow flight. The rise from the dip is more steep until an inflection point, where the curve takes an asymptotic behaviour, tending to the flutter speed of the pitch-plunge system.

This behaviour is exhibited in figures from 8 to 15. The next V-g plots (figure 7) explain the cause of the dip. The V- ω graph shows how flap and plunge natural frequencies coalesce at an almost zero speed. In absence of flap, flutter speed would be much higher, when pitch and plunge frequencies coalesce. On the other hand, the V-g shows that the fictitious damping that becomes positive is the one corresponding to pitch. Hence, a triple interaction occurs. As g is positive from the beginning, this is a mild-flutter case. It would be easily removed with the addition of damping.

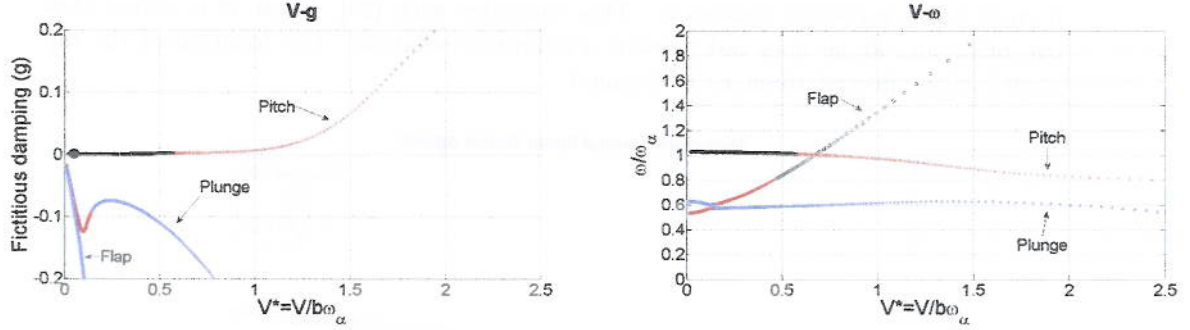


Figure 7: $V\text{-}g$ and $V\text{-}\omega$ graphs for a pitch-plunge-flap aerofoil. $\frac{\omega_\beta}{\omega_\alpha} = 0.67$ and $\kappa = 0.2$

- *Effect of location of aerofoil center of gravity, x_α .* From figure 8 it can be deduced that the position of the center of gravity alters mainly the asymptotic behaviour of the flutter speed at large values of $\omega_\beta/\omega_\alpha$. As x_α is increased, the maximum value of the flutter onset is significantly reduced, whereas the minimum value remains almost constant and very close to zero. The dip is slightly displaced leftwards in the graph as x_α is increased. The general behaviour of the curves does not change.

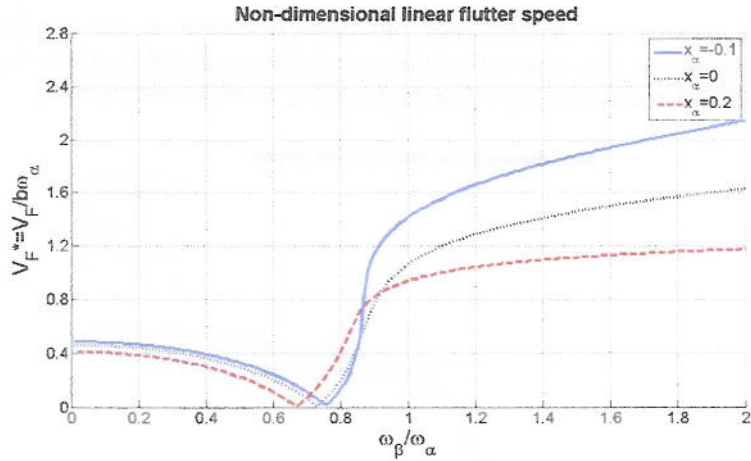


Figure 8: Influence of x_α on flutter speed

- *Effect of flap center of gravity, x_β .* Figure 9 shows the influence of moving the location of the flap's mass center. The most remarkable effect is that if $x_\beta < 0$, the minimum flutter speed experiments a significant increase. A further increase in the mass balance of the flap (x_β more negative) leads to a softer dip, even though

it does not completely remove it. This coincides with [23], where it is stated that overbalancing alone does not present a definitive solution. The location of the dip itself is also affected when x_β is changed.

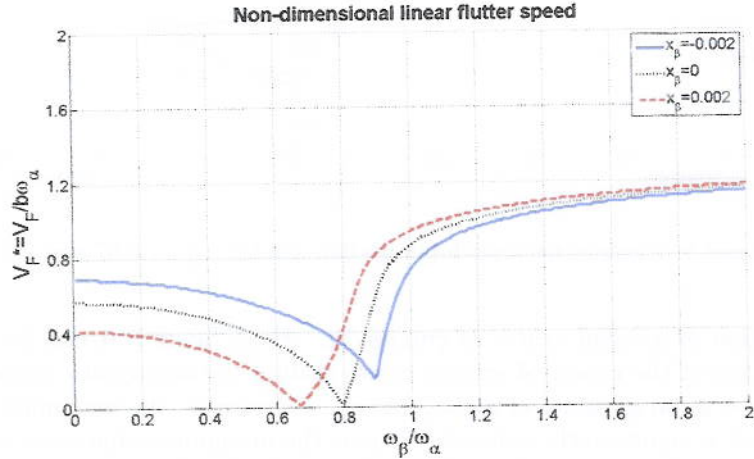


Figure 9: Influence of x_β on flutter speed

- *Effect of pitch inertia, r_α .* In this case too there is a shift of the dip (figure 10). On the other hand, as the moment of inertia of the aerofoil-flap grows ($r_\alpha \uparrow$), the asymptotic value of the flutter speed at high $\omega_\beta / \omega_\alpha$ is increased as well.

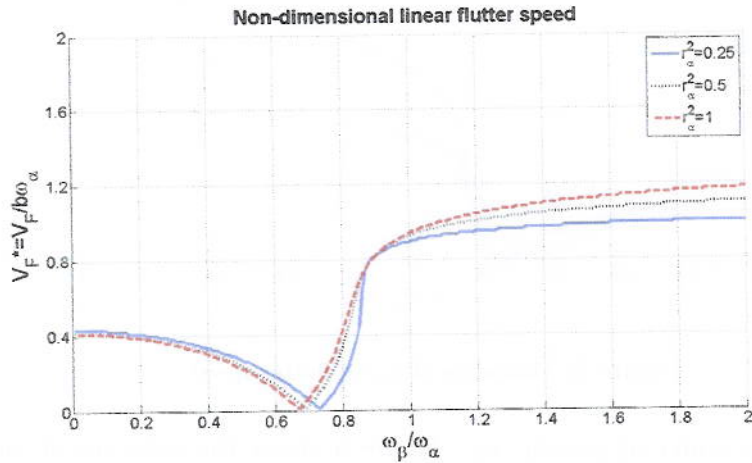


Figure 10: Influence of r_α on flutter speed

- *Effect of flap pitch inertia, r_β .* The flutter onset at low values of ω_b/ω_α is reduced as r_β decreases (figure 11). Besides, the location of the dip is displaced. The asymptotic behaviour is not affected.

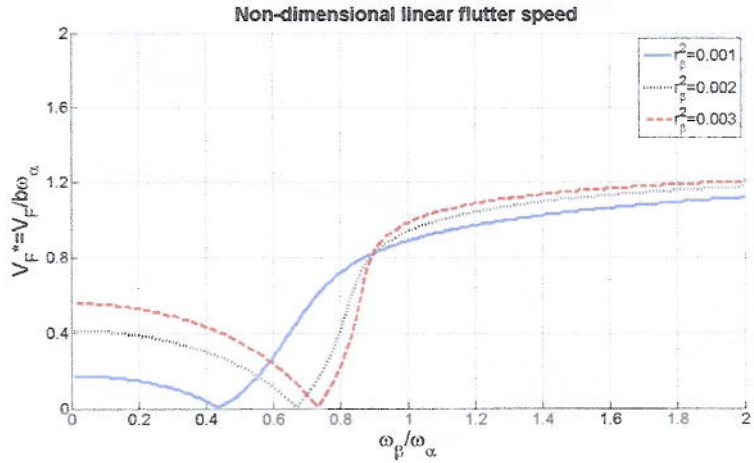


Figure 11: Influence of r_β on flutter speed

- *Effect of elastic axis position, a .* The dip location is affected, but not its value (figure 12). Besides, the variation is relatively small compared to the change in the value of a . In contrast, there is appreciable influence over the asymptotic tendency.

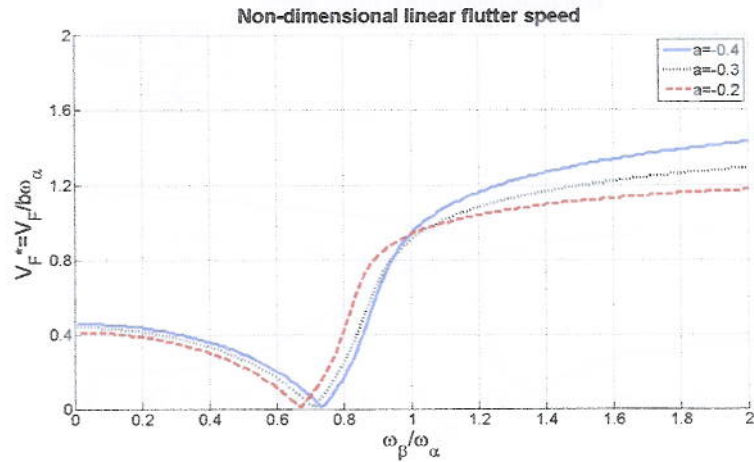


Figure 12: Influence of a on flutter speed

- *Effect of hinge position, c.* As figure 13 shows, a minute change originates strong changes in most of the frequency ratio range. However, the asymptotic value remains unaffected, as well as the standard shape.

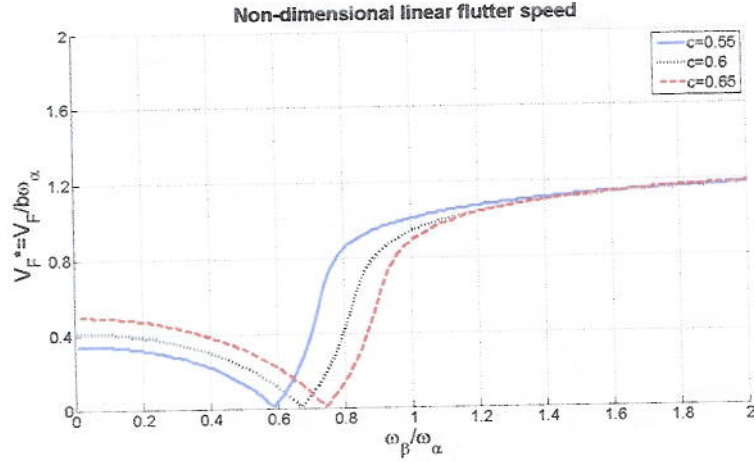


Figure 13: Influence of c on flutter speed

- *Effect of ω_h/ω_α .* Figure 14 shows the important role of this ratio. As it is increased, the asymptotic value is reduced. As the ratio tends to unity, the behaviour of the curve changes drastically and the typical shape cannot be recognized anymore.

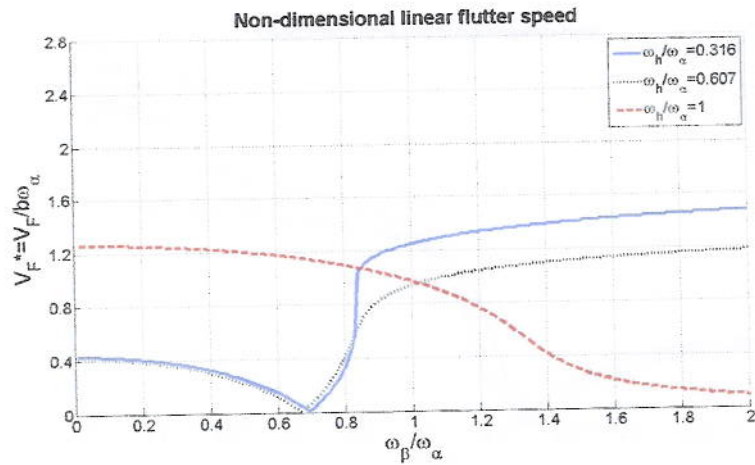


Figure 14: Influence of ω_h/ω_α on flutter speed

- *Effect of κ .* The influence of this parameter turns out to be crucial. As can be seen in figure 15, not only does the asymptotic behaviour change, but the dip is also critically affected. In fact, the dip can be softened to a extent where the minimum flutter velocity is nearly the same as the average value at low frequency ratios. Hence, flight altitude and aerofoil mass are determinant.

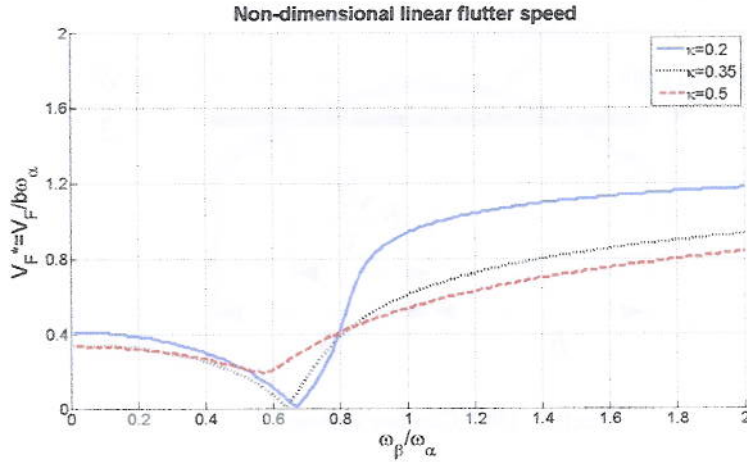


Figure 15: Influence of κ on flutter speed

3.2 Analysis of camber effects

In this section, pitch, plunge and camber degrees of freedom are considered. The relevant equations of motion are (16-18) and flap deflection β is dismissed in the aerodynamic loads. As aforementioned, an homogeneous flat plate with $a = 0$ and $x_\alpha = 0$ is assumed. For this system, the set of parameters that univocally determines the flutter problem is

$$\frac{\omega_h}{\omega_\alpha}, \frac{\omega_\delta}{\omega_\alpha}, \kappa \quad (45)$$

The main objective of this section is to investigate the mechanisms that lead to instability under different conditions. For this purpose, different tools have been used, being V -graphs and eigenvector analysis the most helpful. The analysis follows an increasing complexity approach, starting with a single-degree of freedom system. Then, all possible combinations of two degrees of freedom are studied: pitch-plunge, pitch-camber and plunge-camber. Finally, the system comprising the three modes is considered.

3.2.1 One degree of freedom

Let us consider the camber degree of freedom alone. For this purpose, only equation (18) is required. Figure 16 illustrates the physical system, where the plate is fixed at two symmetric points, at a distance $b\frac{\sqrt{3}}{3}$ from the midchord. This value comes from the assumed bending parabolic mode (10).

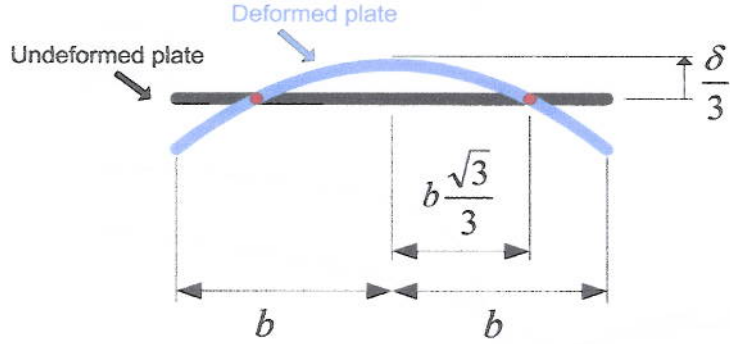


Figure 16: Camber system

Appending the unsteady aerodynamic camber bimoment given by equation (23) and removing all dependencies with respect to other degrees of freedom, the equation of motion for camber-only degree of freedom system is

$$\left(1 + \frac{45}{4} \frac{1}{36} \kappa\right) \frac{\ddot{\delta}}{b} + \frac{45}{4} \frac{1}{18} \kappa \frac{V}{b} C(k) \frac{\dot{\delta}}{b} + \left[\omega_\delta^2 - \frac{45}{4} \left(\frac{1}{2} - \frac{1}{3} C(k)\right) \kappa \left(\frac{V}{b}\right)^2 \right] \frac{\delta}{b} = 0 \quad (46)$$

Steady and quasi-steady analyses First of all, the steady case is studied. This is obtained neglecting the time-derivatives and setting $C(k) = 1$ in equation (46). The non-trivial solution of the resulting equation gives the non-dimensional divergence speed

$$V_D^* = \frac{V_D}{\omega_\delta b} = \sqrt{6 \frac{4}{45} \frac{1}{\kappa}} \quad (47)$$

On the other hand, as an intermediate step between unsteady and steady analyses, quasi-steady approximation is considered next. For this purpose, Theodorsen's function is set to unity but time-derivatives are not ignored. This approximation means that the unsteady wake is completely disregarded. There is no flutter speed in this case, and divergence is reached first. This seems to imply that the wake is the only responsible for flutter; neglecting it means that the mechanism leading to dynamic instability is disabled and hence, flutter does no longer occur. The unsteady analysis further proves this statement.

Unsteady analysis Defining the following coefficients that only depend on κ

$$a'_2 = 1 + \frac{45}{4} \frac{1}{36} \kappa \quad (48)$$

$$a'_1 = \frac{45}{4} \frac{1}{18} \frac{\kappa}{b} \quad (49)$$

$$a'_{01} = \frac{45}{4} \frac{1}{2} \frac{\kappa}{b^2} \quad (50)$$

$$a'_{02} = \frac{45}{4} \frac{1}{3} \frac{\kappa}{b^2} \quad (51)$$

and assuming harmonic motion of the form $\delta = \delta_0 e^{i\omega t}$, equation (46) reduces to

$$[-\omega^2 a'_2 + i\omega a'_1 V C(k) + \{\omega_\delta^2 - [a'_{01} - a'_{02} C(k)] V^2\}] \delta_0 = 0 \quad (52)$$

Flutter will occur when the term within square brackets multiplying δ_0 equals zero. This requires both the real and imaginary part of the equation to be zero. Theodorsen's function can be expanded as real and imaginary part

$$C(k) = F(k) + iG(k) \quad (53)$$

where $F(k)$ and $G(k)$ are known combinations of Bessel functions. Hence, the following two equations are obtained for the real and imaginary part respectively

$$-\omega^2 a'_2 - \omega a'_1 G(k)V + \{\omega_\delta^2 - [a'_{01} - a'_{02} F(k)] V^2\} = 0 \quad (54)$$

$$\omega^2 a'_1 F(k)V + \omega a'_2 G(k)V^2 = 0 \quad (55)$$

Equation (55) yields

$$\frac{\omega}{V} = -\frac{a'_{02}}{a'_1} \frac{G(k)}{F(k)} \quad (56)$$

Recalling the expression of the reduced frequency k (27) and substituting the values of the coefficients (48-51)

$$k = -6 \frac{G(k)}{F(k)} \quad (57)$$

This result shows that, for the camber single degree of freedom system, flutter occurs for a constant value of k , irrespective of the rest of the parameters of the problem. Note that the ratio $\frac{G}{F}$ represents the argument of Theodorsen's complex function. It can be understood as the phase shift between the quasi-steady and the circulatory aerodynamic loads, where the latter lags the former [8].

As a result, flutter is entirely determined by $C(k)$, which as stated before, represents the influence of the shed wake over the aerofoil. This explains the mechanism of flutter in this case. In classical aeroelasticity, flutter is due to the interchange of energy between two vibration modes, namely pitch and plunge. These degrees of freedom are inherently stable if considered independently [1]. In contrast, the camber degree of freedom does not require any other mode for flutter to occur; it is the interaction between the wake and the aerofoil what causes instability. In other words, oscillations are amplified extracting energy from the wake.

The value of the proportionality constant between the reduced frequency and the argument of the wake function arises from the derivation of aerodynamic bimoment, based on a Chebyshev expansion [7]. Explaining its origin would require further study, which is out of the scope of this project.

On the other hand, the constant value of reduced frequency at which flutter occurs leads to a non-dimensional flutter velocity that only depends on κ . After some manipulation and substitution of numerical values, equation (54) leads to the following relationship

$$V_F^* = \frac{V_F}{\omega_\delta b} \approx \frac{1}{\sqrt{1.15 + 3.80\kappa}} \quad (58)$$

Note that comparison between equations (58) and (47) shows that flutter will always happen before divergence in the unsteady case of a single degree of freedom system.

Finally, relevant V-g and V- ω plots are presented in figure 17.

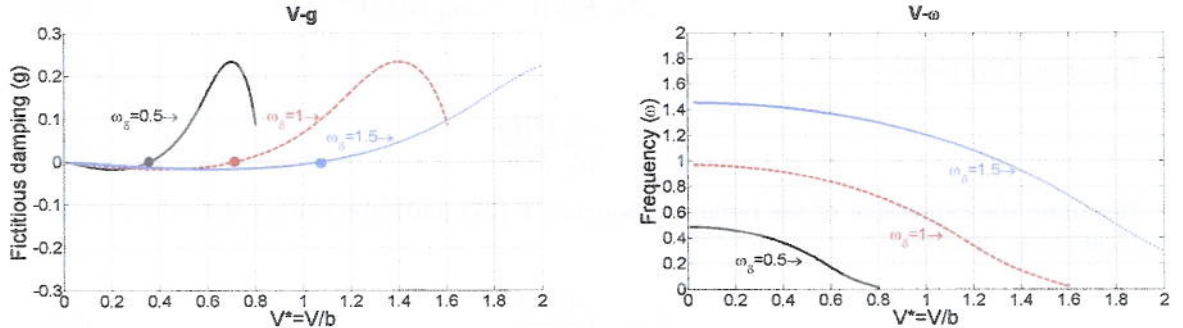


Figure 17: V-g and V- ω graphs for the camber degree of freedom. $\kappa = 0.2$

The flutter speed is determined by the point where the damping curve in the V-g graph crosses the x -axis. It corresponds to the value given by equation (58). Obviously, no frequency coalescence can be seen, since the system consists of only one degree of freedom.

On the other hand, the velocity at which the frequency curve crosses the x -axis in the $V-\omega$ plot corresponds to the divergence speed, given by equation (47). It can also be observed in the $V-\omega$ graph that at zero speed the frequency matches the natural camber frequency.

3.2.2 Two degrees of freedom

In order to interpret the mechanisms of flutter when three degrees of freedom are considered, it is interesting to look at what happens when only two of them interact. For this purpose, pitch-plunge, camber-pitch and camber-plunge combinations are studied next.

Pitch and plunge Classical flutter analysis comprises pitch and plunge degrees of freedom. This problem has been widely studied and reported in the bibliography, so only a very quick overview will be considered here, necessary for the sections to follow. Note that the structural model introduced in section 2.1.2 (flat plate attached at its midchord) has been used to obtain the results, in contrast to figure 5. This model is shown in figure 18.

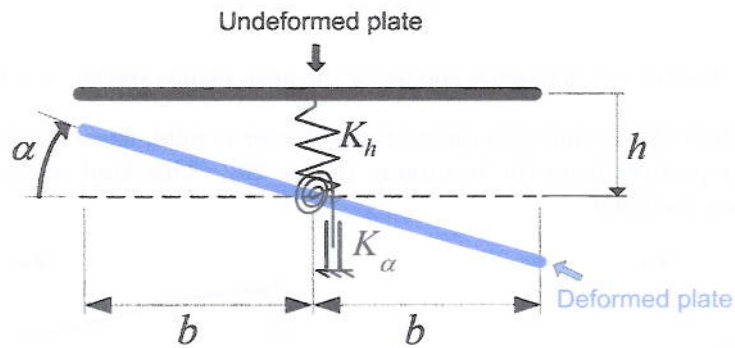


Figure 18: Pitch-plunge system

Figure 19 shows flutter speed for the pitch and plunge system, both unsteady and quasi-steady cases. Besides, divergence speed is included.

For $\frac{\omega_h}{\omega_\alpha} > 0.85$, the flutter speed goes to infinity. But one of the most significant features of this graph is that, for the structural model considered, flutter would never occur, not even for $\frac{\omega_h}{\omega_\alpha} < 0.85$. Divergence is always reached first.

On the other hand, it can be observed that in the absence of wake (quasi-steady approximation), the system would be inherently unstable for low values of the $\frac{\omega_h}{\omega_\alpha}$ ratio.

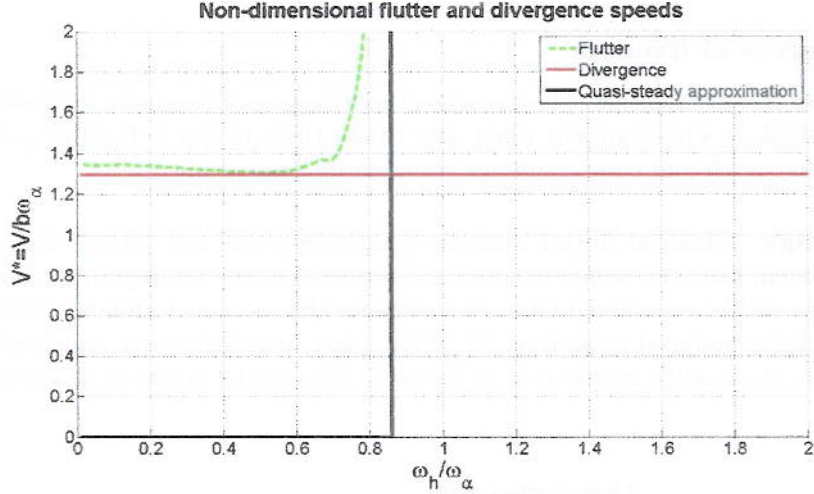


Figure 19: Flutter and divergence speeds for the pitch-plunge system. $\kappa = 0.2$

However, a V-g analysis shows that this quasi-steady flutter is mild, since the value of the fictitious damping is positive from the beginning (figure 20). This kind of flutter would vanish if damping was included.

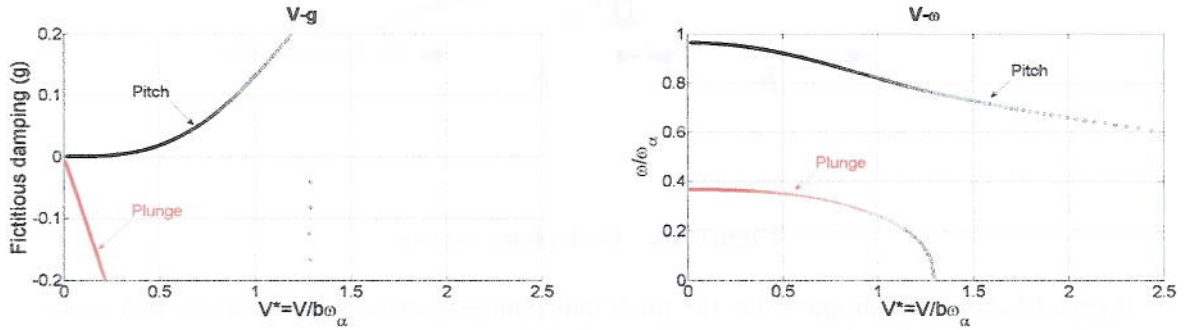


Figure 20: V-g and V- ω graphs for a pitch-plunge aerofoil. Quasi-steady approximation. $\frac{\omega_h}{\omega_\alpha} = 0.4$ and $\kappa = 0.2$

Hence, the presence of the wake somehow stabilizes the system, acting as aerodynamic damping. This can be clearly seen in the V-g plot of the unsteady case (figure 21), where the fictitious damping (g) starts being negative.

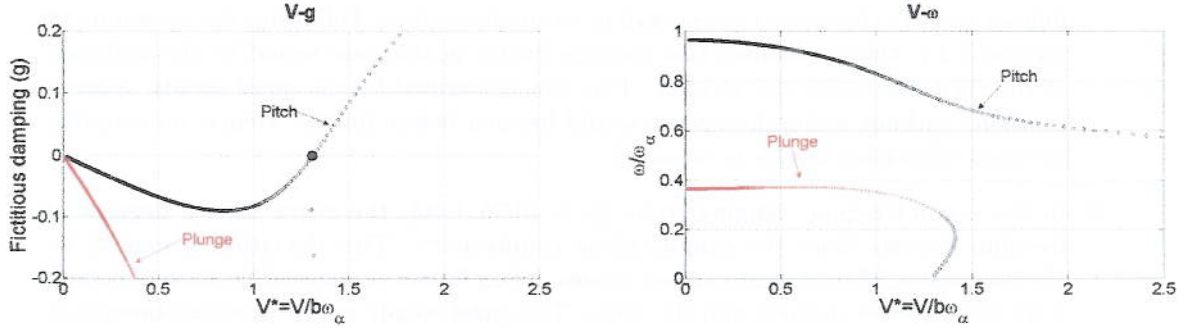


Figure 21: $V\text{-}g$ and $V\text{-}\omega$ graphs for a pitch-plunge aerofoil. $\frac{\omega_h}{\omega_\alpha} = 0.4$ and $\kappa = 0.2$

Pitch and camber For the system consisting of pitch and camber degrees of freedom, equations (16) and (18) are considered. Hence, there is neither plunge nor lift present. Figure 22 illustrates the model:

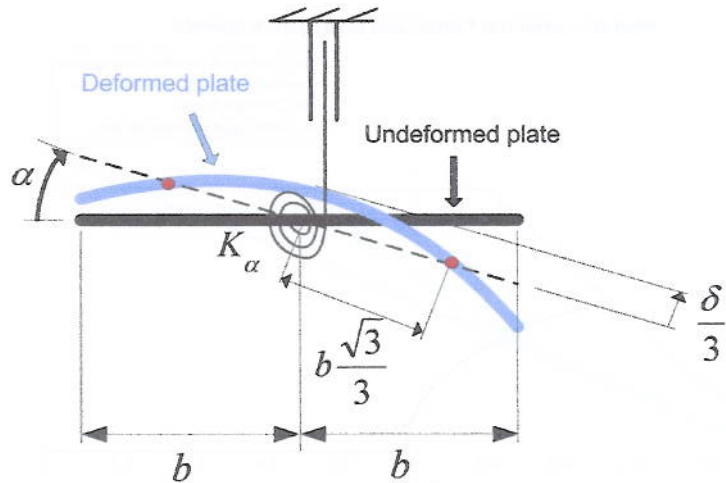


Figure 22: Camber-pitch system

Figure 23 shows the evolution of both flutter and divergence speeds for the two-degrees-of-freedom system. Flutter speed for the camber-only system and quasi-steady approximation are also presented to help to interpret results. The camber-pitch aerofoil exhibits a behaviour that can be clearly divided into three main zones:

1. In the first one, flutter is governed by camber. The flutter curve of pitch and camber

follows exactly the curve corresponding to single camber. Following the reasoning of section 3.2.1, the mechanism that governs flutter in this case would be the influence of the shed wake over the aerofoil. This can be verified by the quasi-steady approximation: without wake, divergence would happen before flutter. Hence, no coupling between vibrations modes is expected.

2. In the second region, ranging from $\frac{\omega_\delta}{\omega_\alpha} \in [0.56, 1.40]$, the curve of two degrees of freedom departs from the camber-alone counterpart. This deviation is caused by the interaction of pitch and camber modes, being flutter originated because of energy interchange between them and the wake. The quasi-steady approximation shows that the wake might be stabilizing the situation.
3. Finally, there is a last zone where flutter no longer occurs for the pitch-camber combination. In this case divergence speed is reached first, so the static phenomena imposes the stability boundary. This is likely to be due to pitch command. As stated before, single pitch is inherently stable, so if this degree of freedom governs the behaviour, absence of flutter is reasonable.

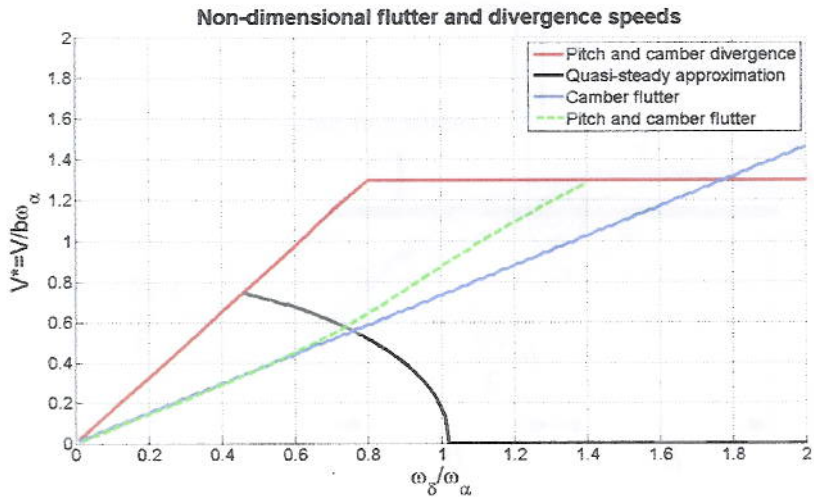


Figure 23: Flutter and divergence speeds for the pitch-camber system. $\kappa = 0.2$

Eigenvector and V-g analyses shed some light into the problem. For suitable frequency ratios in each region, the eigenvectors expressed as modulus and argument are given in table 2. In the first region, the magnitude of the camber eigenvector is much larger than the pitch eigenvector, and it is who controls flutter. In contrast, for $\omega_\delta/\omega_\alpha = 1$, both eigenvectors have moduli of the same order of magnitude, and the phase shift exhibited verifies that

both modes are coupled and interchanging energy. Note that in the absence of wake this coupling remains, but the phase shift is modified.

The magnitude of v_α increases gradually in the unsteady case without sudden discontinuities, and this accounts for a smooth transition between the two flutter mechanisms. For the limiting value beyond which flutter does not exist, i.e., $\omega_\delta/\omega_\alpha = 1.4$, both eigenvectors are almost in counter-phase. The quasi-steady eigenvectors at this point prove that pitch gradually starts to govern the system. Hence after, pitch-control is complete and no flutter is found.

$\omega_\delta/\omega_\alpha$	v_α	v_δ	v_α	v_δ
0.50	0.04 132°	1 0°	0.05 -90°	1 0°
1.00	0.46 -152°	0.88 0°	0.66 -91°	0.75 0°
1.40	0.73 0°	0.68 177°	1 0°	0.007 92°
Unsteady		Quasi-steady		

Table 2: Eigenvectors. Pitch and camber degrees of freedom

V-g and V- ω plots for the unsteady case are presented next. The curves are very similar in the first two regions, but with important peculiarities. In the first case (figure 24), the damping curve corresponding to camber becomes zero. On the contrary, it is the pitch damping curve which crosses the x-axis in figure 25. This verifies the hypothesis that flutter is caused by camber only in the first region and by mode interaction in the second.

The damping curve is always negative in figure 26, and hence flutter never occurs. In figures 24 and 25, frequencies tend to coalesce: at approximately flutter speed, the lower curve has an inflexion point. This is obviously not true for the figure 26, where both curves depart.

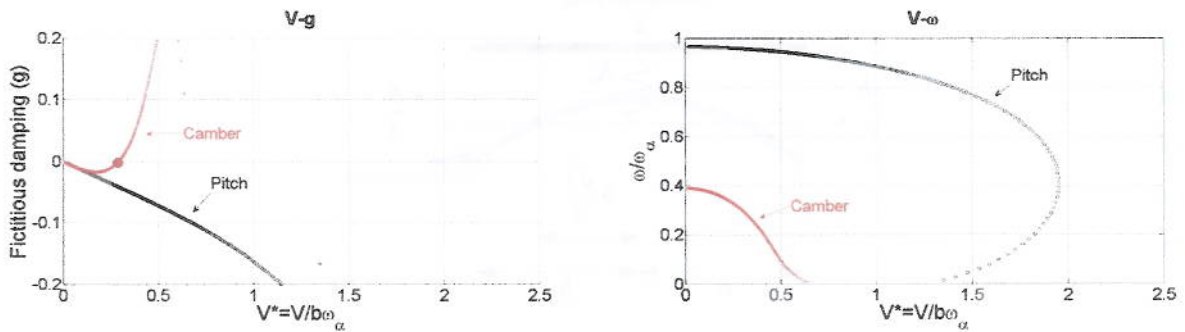


Figure 24: V-g and V- ω graphs for a pitch-camber aerofoil. $\frac{\omega_\delta}{\omega_\alpha} = 0.4$ and $\kappa = 0.2$

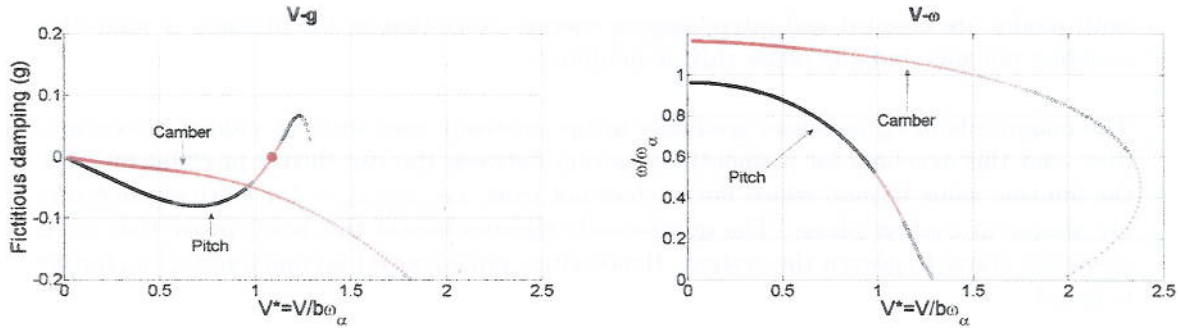


Figure 25: V-g and V- ω graphs for a pitch-camber aerofoil. $\frac{\omega_b}{\omega_\alpha} = 1.2$ and $\kappa = 0.2$

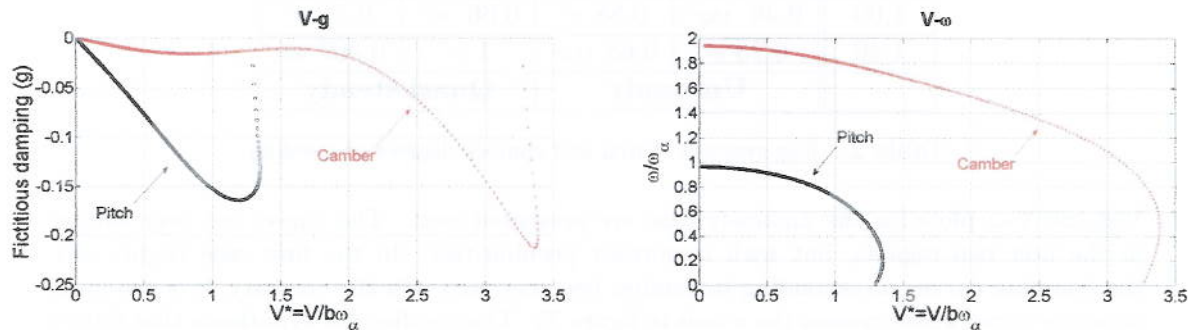


Figure 26: V-g and V- ω graphs for a pitch-camber aerofoil. $\frac{\omega_b}{\omega_\alpha} = 2$ and $\kappa = 0.2$

Plunge and camber Figure 27 illustrates the model:

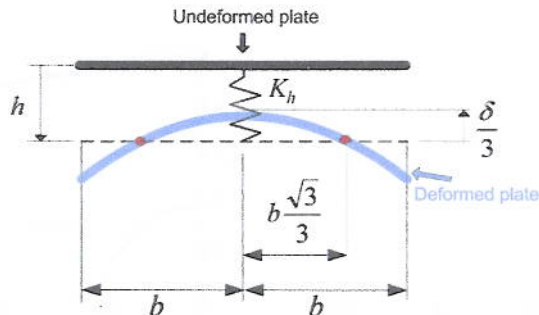


Figure 27: Camber-plunge system

For this system, only equations (17-18) are considered. The camber-plunge aerofoil mani-

tests a radically different behaviour compared to the camber-pitch case. Figure 28 shows the comparison of plunge-camber and camber-only flutter speeds. In this case there is no divergence speed.

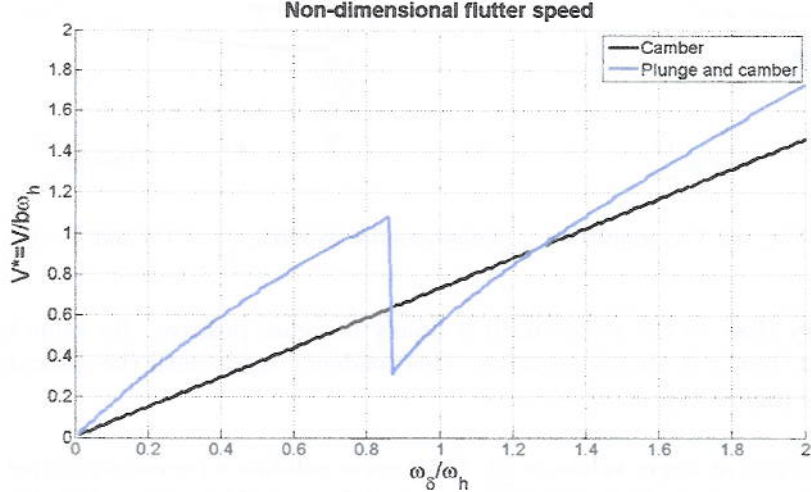


Figure 28: Flutter speeds for the plunge-camber system. $\kappa = 0.2$

As shown in figure 28, there is a discontinuity in the flutter curve. This abrupt jump is likely to be caused by the structural coupling between both degrees of freedom. In fact, it has been found that the discontinuity occurs at approximately $\frac{\omega_\delta}{\omega_h} = \sqrt{\frac{4}{5}}$. Note that, from equation (18), an 'effective' camber natural frequency can be considered

$$\omega_\delta'^2 = \omega_\delta^2 + \frac{5}{4}\omega_h^2 \quad (59)$$

V-g and V- ω graphs allow gaining more insight into the problem. Figure 29 shows characteristic plots. The first peculiarity is that the frequency plot at $V^* = 0$ does not show the natural frequencies of the single modes ω_δ and ω_h . This is due to the structural coupling between plunge and camber. Following an eigenvalue analysis, it can be proved after some algebra that the natural frequencies of this system are given by

$$\omega^2 = \frac{1}{2}\omega_\delta^2 + \frac{9}{8}\omega_h^2 \pm \sqrt{\left(\frac{1}{2}\omega_\delta^2 + \frac{9}{8}\omega_h^2\right)^2 - (\omega_\delta\omega_h)^2} \quad (60)$$

which match the plotted values at zero velocity.

On the other hand, plots in figure 29 correspond to $\frac{\omega_\delta}{\omega_h} = 1.5$, but the form of them does not change over the range of frequency ratios considered. As can be seen, one of the damping

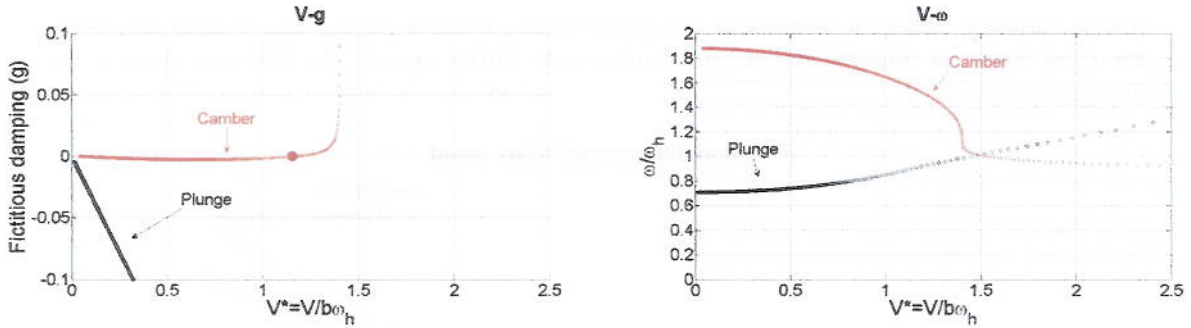


Figure 29: V-g and V- ω graphs for a plunge-camber aerofoil. $\frac{\omega_\delta}{\omega_h} = 1.5$ and $\kappa = 0.2$

modes remains very close to the x -axis until it finally becomes positive. Its value is very small till this point, but it is always negative. This tendency holds until the discontinuity of the flutter curve (figure 28).

At the discontinuity and at larger values of $\frac{\omega_\delta}{\omega_h}$, the g curve exhibits a previous positive peak, turning negative again and finally crossing the x -axis definitely. The values of g when they first become positive are of the order of 10^{-6} or less. If these values were considered zero (round error), the flutter curve would be smooth. The addition of structural damping in camber as small as one per cent removes the discontinuity, too. Finally, the discontinuity becomes a dip if the quasi-steady approximation is considered.

The eigenvectors of the system are presented in table 3.

ω_δ/ω_h	v_h	v_δ
0.4	0.26 0°	1 0°
0.86	0.18 16°	1 0°
0.87	0.15 180°	1 0°
1.35	0.04 172°	1 0°
1.8	0.12 14°	1 0°

Table 3: Eigenvectors. Plunge and camber degrees of freedom

Finally, figure 30 compares the original flutter curve presented in figure 28 with the curves obtained considering quasi-steady approximation, damping and reduced accuracy.

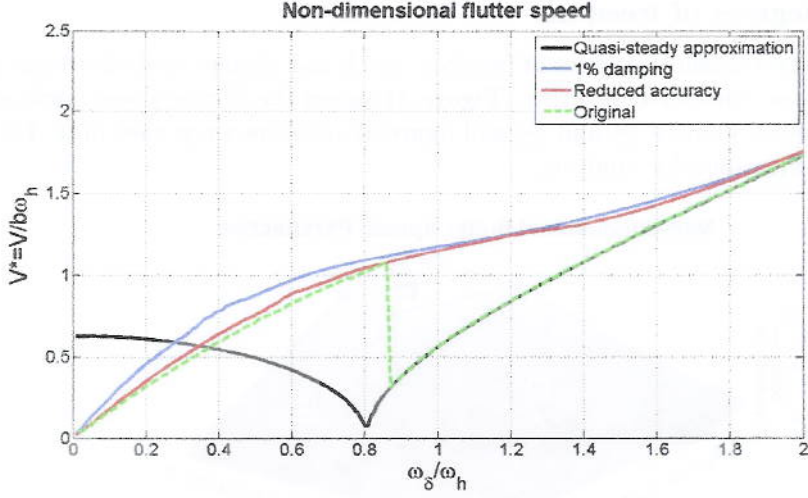


Figure 30: Comparison of different approximations to the flutter speed. $\kappa = 0.2$

All this information suggests complex flutter mechanisms. The structural coupling makes the physics not as obvious as in the pitch-camber case. The following explanation might be plausible:

1. Strikingly, the eigenvectors right before and after the discontinuity exhibit the same behaviour. Hence, flutter seems to be driven by the same mechanism in both cases.
2. However, the quasi-steady flutter curve indicates that the influence of the wake is negligible after the dip, whereas it entirely changes the behaviour before it.
3. Apparently, flutter is originated by the energy exchange between both vibration modes, but the wake also contributes before the discontinuity arrives. After it, only mode interaction controls instability.
4. If the wake is ignored, the discontinuity becomes a dip in the curve, still being a critical point. This suggests that this point is likely to be determined by the structural coupling.
5. The stability boundary after the dip seems a neutral stability curve. Fictitious damping reaches zero but does not become positive (within round error). The velocity that makes the system unstable is reached later, leading to a smooth flutter curve.
6. In the neighbourhood of the interception point between plunge-camber and camber-only flutter curves ($\frac{\omega_\delta}{\omega_h} = 1.35$ in figure 28), the magnitude of the plunge eigenvector reduces. It is the only moment when camber presumably governs flutter alone.

3.2.3 Three degrees of freedom

In this section the two classical degrees of freedom -pitch and plunge- and chordwise deformations -camber- are considered together. Figure 31 shows the flutter speed surfaces as a function of the frequency ratios $\frac{\omega_h}{\omega_\alpha}$ and $\frac{\omega_\delta}{\omega_\alpha}$ and figure 32 presents a top view of it. Different regions have been identified for analysis.

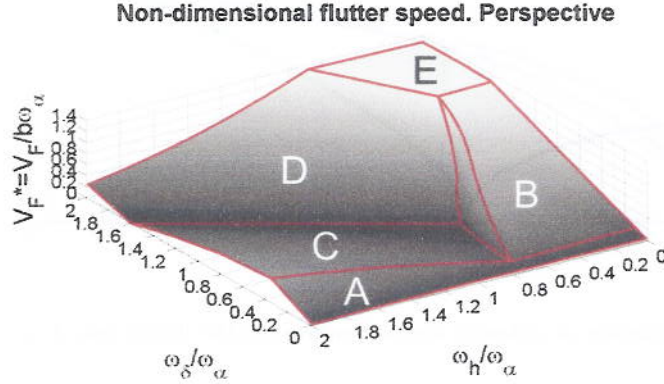


Figure 31: Flutter speed surfaces for a camber-pitch-plunge system. $\kappa = 0.2$

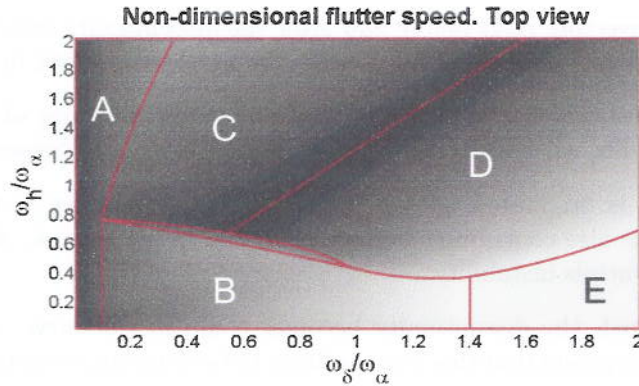


Figure 32: Top view of flutter surfaces for a camber-pitch-plunge system. $\kappa = 0.2$

Some clear trends and characteristic curves are manifested by these surfaces. However, in order to make it simpler and easier to visualize, the analysis will be carried out considering relevant 2D curves and comparing them to simpler systems with two degrees of freedom.

Five main regions can be distinguished in figures 31 and 32, denoted by A, B, C, D and E.

For low values of $\frac{\omega_h}{\omega_\alpha}$, flutter curves increase gradually with $\frac{\omega_h}{\omega_\alpha}$ (region A and B) until an upper plateau is reached (region E). This plateau corresponds to the divergence speed of the system and this is why a discontinuity appears. On the other hand, for values of the frequency ratio spanning from $\frac{\omega_h}{\omega_\alpha} = 0.78$ on, flutter speed exhibits a different behaviour, characterized by a short growth (region A), a discontinuity and a deep valley (regions C and D).

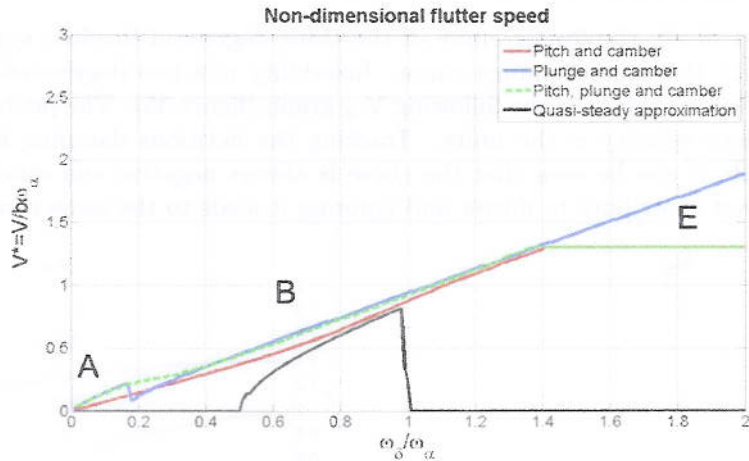


Figure 33: Flutter speed. $\frac{\omega_h}{\omega_\alpha} = 0.2$ and $\kappa = 0.2$

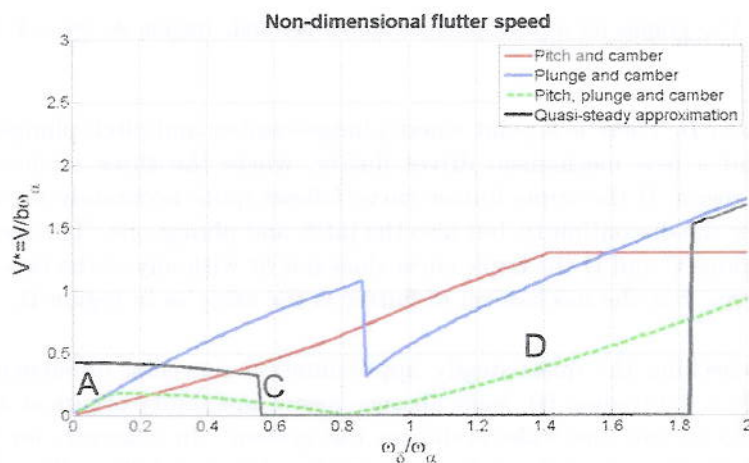


Figure 34: Flutter speed. $\frac{\omega_h}{\omega_\alpha} = 1$ and $\kappa = 0.2$

Figures 33 and 34 show distinctive 2D curves, plotted for relevant values of $\frac{\omega_h}{\omega_\alpha}$. In addition to the curve corresponding to three degrees of freedom, pitch-camber and plunge-camber curves are presented to aid interpretation, as well as quasi-steady approximations.

Although they look like quite different, there are common features to both of them. In fact, the behaviour is very similar and it can be split into three regions, with two different flutter mechanisms and divergence, separated by discontinuities:

1. *Region A.* First of all, the flutter curve of the three degrees-of-freedom system fits in perfectly with the camber-plunge curve. Instability is a two degrees-of-freedom phenomena. This is obvious in the following V-g graph (figure 35). The pitch natural frequency at zero velocity is the unity. Tracking the fictitious damping from the frequency graph, it can be seen that the curve is always negative and quickly goes away. It does not contribute to flutter and ignoring it leads to the same result.

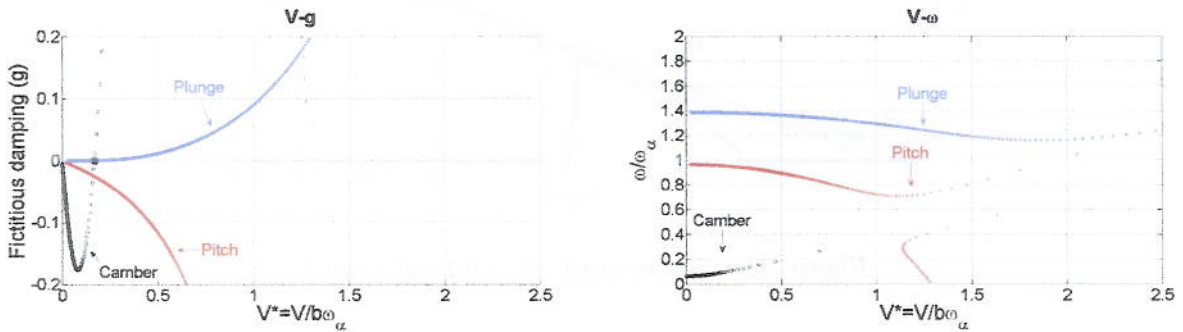


Figure 35: V-g and V- ω graphs for a pitch-plunge-camber aerofoil. Region A. $\frac{\omega_h}{\omega_\alpha} = 1$, $\frac{\omega_\delta}{\omega_\alpha} = 0.1$ and $\kappa = 0.2$

2. *Regions B, C and D.* There is a point where plunge-camber and pitch-plunge-camber curves split and a new mechanism drives flutter, where the three modes interact altogether. In region B the triple flutter curve follows quite accurately the camber-plunge one after the discontinuity, but also the pitch and plunge one. The mechanism is triple. In regions C and D the triple curve does not fit with any of the two-degrees-of-freedom curves, but the mechanism of flutter is the same as in region B.

Nevertheless, checking the quasi-steady approximation a crucial difference can be noticed. For $\frac{\omega_h}{\omega_\alpha} = 0.2$ (region B), wake absence means instability occurs at a slightly lower speed. So to say, the wake stabilizes the system. In contrast, for $\frac{\omega_h}{\omega_\alpha} = 1$ (regions C and D) the role of the wake is reversed and it destabilizes. The unsteady curves are smooth along this region, and recall that structural damping would remove the discontinuities from the quasi-steady ones.

Figure 36 shows typical V-g and V- ω plots of regions B, C and D:

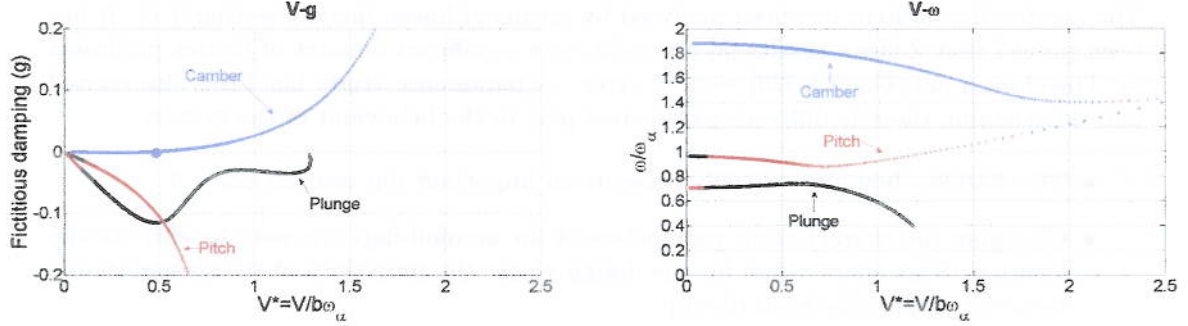


Figure 36: V-g and V- ω graphs for a pitch-plunge-camber aerofoil. Region D. $\frac{\omega_h}{\omega_\alpha} = 1$, $\frac{\omega_\delta}{\omega_\alpha} = 1.5$ and $\kappa = 0.2$

The main difference of figure 36 with respect to figure 35 is that at flutter onset the damping curve of pitch is still above the plunge curve. Looking at 36 it can be clearly seen that there is pitch and plunge frequency coalescence near the flutter speed, but it is the camber fictitious curve which gives flutter. Hence, there is a complex interaction among the three modes.

3. *Region E.* As $\frac{\omega_\delta}{\omega_\alpha} \rightarrow 2$, it seems that the flutter curves approach the pitch-camber divergence. Actually, it is the pitch-plunge-camber divergence what occurs, as the eigenvector analysis will later show. Comparing figures 19, 23, 33 and 34 it can be observed that, in fact, pitch-camber divergence at high enough values of $\frac{\omega_\delta}{\omega_\alpha}$ is the same as pitch-plunge divergence. The mechanism that prevails is still pitch-plunge-camber, but flutter lags divergence.

The following eigenvectors confirm the above-stated:

$\omega_\delta/\omega_\alpha$	Region	v_α	v_h	v_δ	Region	v_α	v_h	v_δ
0.1	A	0.006 -145°	0.24 0.7°	1 0°	A	0.008 -146°	0.3 0°	1 0°
0.8	B	0.12 129°	0.84 0°	0.52 -40°	C	0.02 88°	0.17 180°	1 0°
1.5	E	-	-	-	D	0.09 78°	0.09 175°	1 0°
$\frac{\omega_h}{\omega_\alpha} = 0.2$					$\frac{\omega_h}{\omega_\alpha} = 1$			

Table 4: Eigenvectors. Pitch, plunge and camber degrees of freedom

Another remarkable feature is the point at which the minimum occurs. In the range where the flutter speed presents a dip, the minimum always corresponds to an approximate frequency ratio of $\frac{\omega_\delta}{\omega_h} = \sqrt{\frac{4}{5}}$, as mentioned before. If different values of κ are considered, this value changes only slightly, within a ten per cent.

4 Conclusions

The aerofoil-flap system has been analysed by means of linear theory (section 3.1). It has been proved that Zeiler's results [3] are right, so a significant amount of figures published by Theodorsen and Garrick [23] were in error. A parametric study has been also carried out, determining the role different parameters play in the behaviour of the system:

- The stability boundary usually presents an important dip near $\omega_\beta/\omega_\alpha = 1$.
- Changing the characteristic parameters of the aerofoil-flap it is easy to shift the dip location. This offers a tool for the design stage: the properties of the system should be as far as possible from the dip.
- As $\omega_\beta/\omega_\alpha$ increases, the flutter speed tends to an asymptotic value, which corresponds to the flutter speed of the pitch and plunge system. Hence, only the parameters of the aerofoil (a , x_α , r_α) affect this asymptotic value.
- In the low range of $\omega_\beta/\omega_\alpha$ the flap is determinant in stability, so c , x_β and r_β are critical.
- The minimum value of the flutter curves is hardly affected in general, but a sufficient increase in the value of ω_h/ω_α allows the suppression of the dip. The shape of the curve is drastically changed in this case. However, the ratio ω_h/ω_α must be very close to unity to guarantee this change of behaviour, which leads to low flutter speeds in other ranges of $\omega_\beta/\omega_\alpha$.

The influence of chordwise deformations has been studied in different combinations of degrees of freedom (section 3.2). Unlike classical degrees of freedom pitch and plunge, camber mode alone can lead to flutter. Critical velocity always happens at the same reduced frequency, given by equation (57), which implies that camber-wake interaction is the root of flutter. In this single-degree-of-freedom case, dynamic instability takes place at a lower speed than static divergence.

Combinations of pitch, plunge and camber degrees of freedom have been also studied, leading to the following results:

- Using the structural model presented in section 2.1.2, which assumes that the mid-chord point of the flat plate is fixed, the pitch and plunge aerofoil does never lead to flutter, since static divergence is reached first.
- The pitch and camber flutter curve shows a behaviour that can be divided into three clear zones: camber prevails first, followed by mode interaction and divergence respectively.

- The plunge-camber system exhibits a discontinuity in the stability curve. It happens at a frequency ratio that seems to be intimately related to the structural coupling between both degrees of freedom. Flutter is caused by the interaction of both vibration modes, being the wake also determinant. The discontinuity would be removed if just one per cent of structural damping was added.

Finally, the system consisting of three degrees of freedom (pitch, plunge and camber) has been analysed. As figures 31 and 32 illustrate, there are five major zones, corresponding to three different mechanisms:

- *Region A.* Flutter is due to plunge-camber coupling.
- *Regions B, C and D.* In this case, the mechanism driving flutter is the interaction among the three vibrations modes. The wake also plays an important role, stabilizing in region B and destabilizing in regions C and D.
- *Region E.* There is no flutter in this case because divergence speed is reached first.

In short, it has been proved that both flap and camber deformation can change the stability boundaries of the typical aerofoil section with only two classical degrees of freedom. The triple interaction among all modes leads to different values of flutter speed. Flaps have been extensively studied, but the implementation of controlled camber deformations also opens a path in order to delay flutter onset.

5 Further research

In order to improve and complete the analysis, the following ideas are suggested:

- The undertaken study is only computational, depending heavily on models. Particularly, the camber model has been assumed to represent accurately the physical phenomena but this has not been proved. To fully validate the results, experimentation would be required.
- A parametric study for camber, similar to section 3.1.2, could be undertaken. There are mainly two areas to focus on:
 1. The camber model assumes that the elastic axis and center of gravity of the flat plate coincide in the midchord point. It would be interesting to analyse the role played by an offset, which changes parameters such as a , x_α and r_α . For this purpose, new equations of motion must be derived first. In this case, coupling terms arise in the inertia contributions, in contrast to equation (11).
 2. The influence of the mass parameter κ is likely to be crucial. This parameter is inversely proportional to the plate thickness t_p . In principle, as the thickness increases, the flutter speed will also increase. But this has not to be true over the whole range of frequency ratios, since different couplings are likely to influence the stability boundary.
- Several results in the camber effects analysis (section 3.2) remain without a satisfactory explanation. On the one hand, the value of reduced frequency k at which flutter occurs in the single degree of freedom case, given by equation (57). On the other, the frequency ratio at which a discontinuity arises in the plunge-camber case ($\frac{\omega_\delta}{\omega_h} = \sqrt{\frac{4}{5}}$), which matches the minimum of the dip in the pitch-plunge-camber case. To interpret both values the model for camber given in [7] should be carefully analysed. For the former, the Chebyshev expansion that gives rise to the aerodynamic loads must be studied and for the latter, the structural model.
- In order to interpret flutter mechanisms, it would be helpful to undertake an energy approach. Computing the work done by each mode over a period of oscillation, how the energy is transferred from one to another could be seen. This should confirm results obtained by V-g and eigenvector analysis. [34] presents a framework based on conservation of energy that might be useful to start with.
- Damping will always appear in practical applications. It has been proved in this project that the influence on flutter onset is critical. Hence, a more rigorous analysis would be desirable, using estimates of damping coefficients obtained from tests.

- Only unforced oscillations have been considered along this report. Although these are most significant in aeroelastic analysis, external forces can influence stability [29]. In fact, the goal of conformable aerofoils with flaps and chordwise deformations is to curb vibrations and delay flutter onset. Therefore, the inclusion of forcing is another natural step to follow, either appending it directly to the aerodynamic loads given by Theodorsen (20-23) or as an input u in state-space fashion (31).
- Linear unsteady aerodynamics have been only considered. The inclusion of non-linear phenomena, such as dynamic stall, would be the next stage. In order to account for it, the semi-empirical model of Leishman-Beddoes [35] could be implemented, for instance. For the solution, the time-domain method validated for the linear case (section 3.1.1) would be used.
- The influence of compressibility effects could also be studied, which play a major role in the helicopter community. These effects could be easily modeled following the approach taken by Leishman and Nguyen [10], based on the introduction of a compressibility factor, given by

$$\beta = \sqrt{1 - M^2} \quad (61)$$

where M stands for the Mach number.

References

- [1] T. Theodorsen. General theory of aerodynamic instability and the mechanism of flutter. *NACA Report 496*, 1934.
- [2] T. Theodorsen and I. E. Garrick. Mechanism of flutter. A theoretical and experimental investigation of the flutter problem. *NACA Report 685*, 1938.
- [3] T. A. Zeiler. Results of Theodorsen and Garrick revisited. *Journal of Aircraft. Engineering notes*, 37(5):918–920, 2000.
- [4] I. N. Spielberg. The two-dimensional incompressible aerodynamic coefficients for oscillatory changes in airfoil camber. *Journal of Aeronautical Sciences*, 20:432–434, 1953.
- [5] W. P. Rodden and B. Stahl. A strip method for prediction of damping in subsonic wind tunnel and flight flutter tests. *Journal of Aircraft*, 6(1):9–17, 1969.
- [6] M. Gaunaa. Unsteady 2d potential-flow forces on a thin variable geometry airfoil undergoing arbitrary motion. Technical report, Risø National Laboratory, Denmark, 2006.
- [7] R. Palacios and C. E. S. Cesnik. Low-speed aeroelastic modeling of very flexible slender wings with deformable airfoils. In *Proceedings of the 49th AIAA/ASME/ASCE/AHS/ASC Structures, Structural Dynamics and Materials Conference*, Schaumburg, Illinois, USA, April 2008. AIAA 2008-1995.
- [8] R. L. Bisplinghoff, H. Ashley, and R. L. Halfman. *Aeroelasticity*. Addison-Wesley, 1955.
- [9] J. M. R. Graham. *Unsteady aerodynamics with reference to wind turbines*. CENER, 2007.
- [10] J. G. Leishman and K. Q. Nguyen. State-space representation of unsteady airfoil behaviour. *AIAA Journal*, 28(5):836–844, 1989.
- [11] G. Depailler and P. P. Friedmann. Alleviation od dynamic stall induced vibrations using actively controlled flaps. In *Proceedings of the American Helicopter Society 58th Annual Forum*, Montreal, Canada, June 2002. American Helicopter Society, Inc.
- [12] P.P. Friedmann. Aeroelastic scaling for rotary-wing aircraft with applications. *Journal of Fluid and Structures*, 19:635–650, 2004.
- [13] J. Shen. *Comprehensive aeroelastic analysis of helicopter rotor with trailing-edge flap for primary control and vibration control*. PhD thesis, University of Maryland, USA, 2003.

- [14] M. P. Kinzel. Miniature trailing-edge effectors for rotorcraft applications. Master's thesis, Pennsylvania State University, USA, 2004.
- [15] N. Troldborg. Computational study of the Risø-B1-18 airfoil equipped with actively controlled trailing edge flaps. Master's thesis, Technical University of Denmark, 2004.
- [16] P. K. Chavariopoulos. Flap/lead-lag aeroelastic stability of wind turbine blade sections. *Wind Energy*, 2:99–112, 1999.
- [17] S. R. Viswamurthy and R. Ganguli. Effect of piezoelectric hysteresis on helicopter vibration control using trailing-edge flaps. *Journal of Guidance, Control and Dynamics*, 29(5):1201–1209, 2006.
- [18] S. R. Viswamurthy, A. K. Rao, and R. Ganguli. Dynamic hysteresis of piezoceramic stack actuators used in helicopter vibration control: experiments and simulations. *Smart Materials and Structures*, 16:1109–1119, 2007.
- [19] P. B. Andersen, M. Gaunaa, C. Bak, and M. H Hansen. A dynamic stall model for airfoils with deformable trailing edges. *Journal of Physics: Conference Series*, 75, 2007.
- [20] T. Theodorsen. Theory of wing sections of arbitrary shape. *NACA Report 411*, 1931.
- [21] T. Theodorsen. General potential theory of of arbitrary wing sections. *NACA Report 452*, 1932.
- [22] T. Theodorsen and I. E. Garrick. Nonstationary flow about a wing-aileron-tab combination including aerodynamic balance. *NACA Report 736*, 1941.
- [23] T. Theodorsen and I. E. Garrick. Flutter calculations in three degrees of freedom. *NACA Report 741*, 1941.
- [24] H. Wagner. Über die Entstehung des Dynamischen Auftriebes von Tragflügeln. *Zietschrift für Angewandte Mathematik und Mechanick*, 5(1):17, 1925.
- [25] J. G. Leishman. *Principles of helicopter aerodynamics*. Cambridge University Press, 2000.
- [26] J. G. Leishman. Unsteady lift of a flapped airfoil by indicial concepts. *Journal of Aircraft*, 31(2):288–297, 1994.
- [27] N. Hariharan and J. G. Leishman. Unsteady aerodynamics of a flapped airfoil in subsonic flow by indicial concepts. *Journal of Aircraft*, 33(5):855–868, 1996.
- [28] E. H. Dowell. *A modern course in aeroelasticity*. Kluwer Academic Publishers, 2004.

- [29] M. S. Broadhurst, R. Holbach, and J. Lee. Modelling of the non-linear dynamics of an aerofoil section. Technical report, Imperial College London, UK, 2003.
- [30] R. T. Jones. The unsteady lift of a wing of finite aspect ratio. *NACA Report 681*, 1940.
- [31] W. P. Jones. Aerodynamic forces on wings in nonuniform motion. *ARC R and M 2117*, 1945.
- [32] K. J. Åström and R. M. Murray. *Feedback systems*. Princeton University Press, 2008.
- [33] M. J. Patil, R. N. Yurkovich, and D. H. Hodges. Incorrectness of the k method for flutter calculations. *Journal of Aircraft. Engineering notes*, 41(2):402–405, 2003.
- [34] M. J. Patil. From fluttering wings to flapping flight: the energy connection. *Journal of Aircraft*, 40(2):270–276, 2003.
- [35] J. G. Leishman and T. S. Beddoes. A semi-empirical model for dynamic stall. *Journal of American Helicopter Society*, 34(3):3–17, 1989.

A Theodorsen's geometric constants

$$\begin{aligned}
T_1 &= -\frac{1}{3}\sqrt{1-c^2}(2+c^2) + c \cos^{-1}c \\
T_2 &= c(1-c^2) - \sqrt{1-c^2}(1+c^2)\cos^{-1}c + c(\cos^{-1}c)^2 \\
T_3 &= -\left(\frac{1}{8}+c^2\right)(\cos^{-1}c)^2 + \frac{1}{4}c\sqrt{1-c^2}\cos^{-1}c(7+2c^2) \\
&\quad - \frac{1}{8}(1-c^2)(5c^2+4) \\
T_4 &= -\cos^{-1}c + c\sqrt{1-c^2} \\
T_5 &= -(1-c^2) - (\cos^{-1}c)^2 + 2c\sqrt{1-c^2}\cos^{-1}c \\
T_6 &= T_2 \\
T_7 &= -\left(\frac{1}{8}+c^2\right)\cos^{-1}c + \frac{1}{8}c\sqrt{1-c^2}(7+2c^2) \\
T_8 &= -\frac{1}{3}\sqrt{1-c^2}(2c^2+1) + c\cos^{-1}c \\
T_9 &= \frac{1}{2}\left[\frac{1}{3}\left(\sqrt{1-c^2}\right)^3 + aT_4\right] = \frac{1}{2}(-p+aT_4) \\
\text{where } p &= -\frac{1}{3}\left(\sqrt{1-c^2}\right)^3 \\
T_{10} &= \sqrt{1-c^2} + \cos^{-1}c \\
T_{11} &= \cos^{-1}c(1-2c) + \sqrt{1-c^2}(2-c) \\
T_{12} &= \sqrt{1-c^2}(2+c) - \cos^{-1}c(2c+1) \\
T_{13} &= \frac{1}{2}[-T_7 - (c-a)T_4] \\
T_{14} &= \frac{1}{16} + \frac{1}{2}ac
\end{aligned}$$

B Dynamics matrix

The state vector x can be split in different blocks

$$\begin{aligned} \mathbf{x} &= [\alpha \ \beta \ h \ \delta \ \dot{\alpha} \ \dot{\beta} \ \dot{h} \ \dot{\delta} \ z_1 \ z_2 \ z_3 \ z_4 \ z_5 \ z_6]^T \\ &= [r \ \dot{r} \ z_{12} \ z_{34} \ z_{56}]^T \end{aligned}$$

where $r = [\alpha \ \beta \ h \ \delta]^T$, $\dot{r} = [\dot{\alpha} \ \dot{\beta} \ \dot{h} \ \dot{\delta}]^T$ and $z_{i,i+1}$ store the aerodynamic states.

Using equations 33 and 34, the equations of motion with the new aerodynamic states appended to them can be expressed as

$$\begin{bmatrix} I_4 & 0 & 0 & 0 & 0 \\ 0 & M_s - M_a N & 0 & 0 & 0 \\ 0 & 0 & I_2 & 0 & 0 \\ 0 & 0 & 0 & I_2 & 0 \\ 0 & 0 & 0 & 0 & I_2 \end{bmatrix} \begin{bmatrix} \dot{r} \\ \ddot{r}_{12} \\ \ddot{r}_{34} \\ \ddot{r}_{56} \end{bmatrix} = \begin{bmatrix} 0 & I_4 & 0 & 0 & 0 \\ N^T P C_1 + (K_a)_{nc} N - K_s & N^T P \dot{C}_1 + (C_a)_{nc} N & N^T P C_2 & N^T P C_2 & N^T P C_2 \\ Z_{12} & \dot{Z}_{12} & X & 0 & 0 \\ Z_{34} & \dot{Z}_{34} & 0 & X & 0 \\ Z_{56} & \dot{Z}_{56} & 0 & 0 & X \end{bmatrix} \begin{bmatrix} r \\ z_{12} \\ z_{34} \\ z_{56} \end{bmatrix}$$

where I_4 and I_2 represent identity matrices of dimension four and two, respectively. The rest of matrices that have been defined are presented in the next page. Hence, the dynamics matrix of the system is given by

$$A = \begin{bmatrix} I_4 & 0 & 0 & 0 & 0 \\ 0 & M_s - M_a N & 0 & 0 & 0 \\ 0 & 0 & I_2 & 0 & 0 \\ 0 & 0 & 0 & I_2 & 0 \\ 0 & 0 & 0 & 0 & I_2 \end{bmatrix}^{-1} \begin{bmatrix} 0 & I_4 & 0 & 0 & 0 \\ N^T P C_1 + (K_a)_{nc} N - K_s & N^T P \dot{C}_1 + (C_a)_{nc} N & N^T P C_2 & N^T P C_2 & N^T P C_2 \\ Z_{12} & \dot{Z}_{12} & X & 0 & 0 \\ Z_{34} & \dot{Z}_{34} & 0 & X & 0 \\ Z_{56} & \dot{Z}_{56} & 0 & 0 & X \end{bmatrix}$$

There are several points to note here:

- This dynamics matrix corresponds to a system of four degrees of freedom. For any simpler subsystem, only the relevant rows and columns must be considered. For this purpose, the equations of the ignored degree(s) of freedom and the corresponding aerodynamic states must be removed.
- Any structural coupling between flap and camber degrees of freedom has been dismissed.
- Recall that for the structural model of camber, $a = 0$, $x_\alpha = 0$ and $r_\alpha^2 = \frac{1}{3}$.

$$\begin{aligned}
M_s &= \begin{bmatrix} r_\alpha^2 & r_\beta^2 + (c-a)x_\beta & \frac{x_\alpha}{b} & 0 \\ r_\beta^2 + (c-a)x_\beta & r_\beta^2 & \frac{x_\beta}{b} & 0 \\ x_\alpha & x_\beta & \frac{1}{b} & 0 \\ \frac{1}{b} & 0 & 0 & 0 \end{bmatrix} & M_a &= \begin{bmatrix} -\frac{\pi}{2V^2} \left(\frac{1}{8} + a^2 \right) b^2 & \frac{T_7 + (c-a)T_1}{2V^2} b^2 & \frac{\pi ab}{2V^2} & 0 \\ -\frac{T_{13}}{V^2} b^2 & \frac{T_3}{2V^2} \frac{b^2}{\pi} & \frac{-bT_1}{2V^2} & 0 \\ \frac{\pi ab^2}{V^2} & \frac{T_1 b^2}{V^2} & -\frac{\pi b}{V^2} & 0 \\ 0 & 0 & \frac{b}{12V^2} & -\frac{b}{36V^2} \end{bmatrix} \\
K_s &= \begin{bmatrix} \omega_\alpha^2 r_\alpha^2 & 0 & 0 & 0 \\ 0 & \omega_\beta^2 r_\beta^2 & 0 & 0 \\ 0 & 0 & \frac{\omega_h^2}{b} & -\frac{1}{3} \frac{\omega_h^2}{b} \\ 0 & 0 & -\frac{1}{3} \frac{\omega_h^2}{b} & \frac{5}{4} \omega_h^2 + \omega_\delta^2 \end{bmatrix} & (K_a)_{nc} &= \begin{bmatrix} 0 & -\frac{1}{2} (T_4 + T_{10}) & 0 & -\frac{\pi}{2b} \\ 0 & \frac{T_4 T_5 - T_{10}}{2\pi} & 0 & 0 \\ 0 & 0 & 0 & 0 \\ 0 & 0 & 0 & \frac{\pi}{2b} \end{bmatrix} \\
(C_a)_{nc} &= \begin{bmatrix} -\frac{\pi b}{2V} \left(\frac{1}{2} - a \right) & -\frac{b}{2V} \left(T_1 - T_8 + (c-a)T_4 + \frac{1}{2} T_{11} \right) & 0 & -\frac{\pi}{4V} \\ \frac{b}{2V} \left[2T_9 + T_1 - T_4 \left(a - \frac{1}{2} \right) \right] & \frac{b T_4 T_{11}}{4\pi V} & 0 & 0 \\ -\frac{\pi b}{V} & b T_4 & 0 & 0 \\ \frac{b}{3V} & 0 & 0 & 0 \end{bmatrix} \\
C_1 &= \frac{1}{2} \begin{bmatrix} 1 & \frac{T_{10}}{\pi} & 0 & \frac{1}{b} \end{bmatrix} & \dot{C}_1 &= \frac{1}{2} \begin{bmatrix} b \left(\frac{1}{2} - a \right) & \frac{b T_{11}}{2\pi V} & \frac{1}{V} & \frac{1}{6V} \end{bmatrix} & C_2 &= \begin{bmatrix} \frac{b_1 b_2}{2} \left(\frac{V}{b} \right)^2 & (A_1 b_1 + A_2 b_2) \frac{V}{b} \end{bmatrix} \\
Z_{12} &= \begin{bmatrix} 0 & 0 & 0 & 0 \\ 1 & 0 & 0 & 0 \end{bmatrix} & \dot{Z}_{12} &= \begin{bmatrix} 0 & 0 & 0 \\ \frac{b}{V} \left(\frac{1}{2} - a \right) & 0 & \frac{1}{V} \\ 0 & \frac{b T_{11}}{2\pi V} & 0 \end{bmatrix} \\
Z_{34} &= \begin{bmatrix} 0 & 0 & 0 & 0 \\ 0 & \frac{T_{10}}{\pi} & 0 & 0 \end{bmatrix} & \dot{Z}_{34} &= \begin{bmatrix} 0 & 0 & 0 & 0 \\ 0 & \frac{b T_{11}}{2\pi V} & 0 & 0 \end{bmatrix} \\
Z_{56} &= \begin{bmatrix} 0 & 0 & 0 & 0 \\ 0 & 0 & 0 & \frac{1}{b} \end{bmatrix} & \dot{Z}_{56} &= \begin{bmatrix} 0 & 0 & 0 & 0 \\ 0 & 0 & 0 & \frac{1}{6V} \end{bmatrix} \\
P &= \begin{bmatrix} \pi \left(a + \frac{1}{2} \right) \\ -\frac{T_{12}}{2} \\ -2\pi \\ -\frac{\pi}{3} \end{bmatrix} & N &= \frac{\kappa}{\pi} \left(\frac{V}{b} \right)^2 \begin{bmatrix} 2 & 2 & 1 & \frac{45}{4} \\ 2 & 2 & 1 & \frac{45}{4} \\ 2 & 2 & 1 & \frac{45}{4} \\ 2 & 2 & 1 & \frac{45}{4} \end{bmatrix} & X &= \begin{bmatrix} 0 & 1 \\ -b_1 b_2 \left(\frac{V}{b} \right)^2 & -(b_1 + b_2) \frac{V}{b} \end{bmatrix}
\end{aligned}$$

C Validation of algorithms

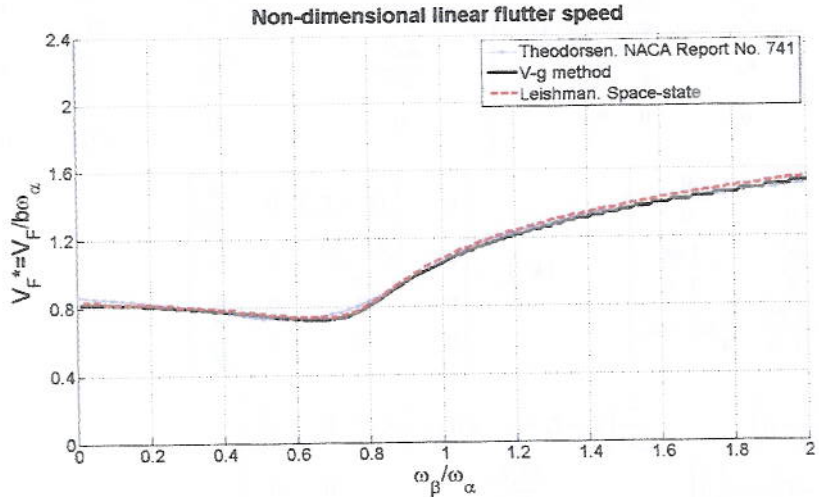


Figure 37: V-g method and Leishman's state-space model against results by Theodorsen and Garrick [23]. $a = -0.2$, $c = 0.6$, $\kappa = 0.2$, $x_\alpha = 0$, $r_\alpha^2 = 1$, $x_\beta = -0.002$, $r_\alpha^2 = 0.002$, $\frac{\omega_h}{\omega_\alpha} = 0.607$

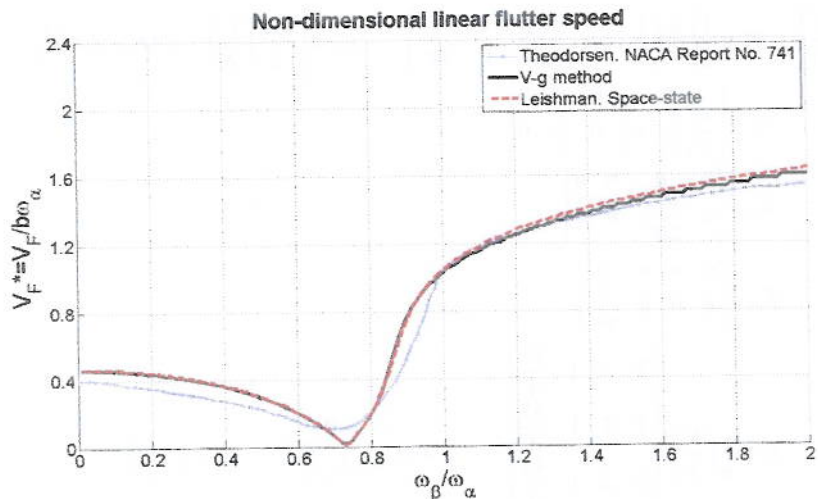


Figure 38: V-g method and Leishman's state-space model against results by Theodorsen and Garrick [23]. $a = -0.2$, $c = 0.6$, $\kappa = 0.2$, $x_\alpha = 0$, $r_\alpha^2 = 1$, $x_\beta = 0.002$, $r_\beta^2 = 0.002$, $\frac{\omega_h}{\omega_\alpha} = 0.607$

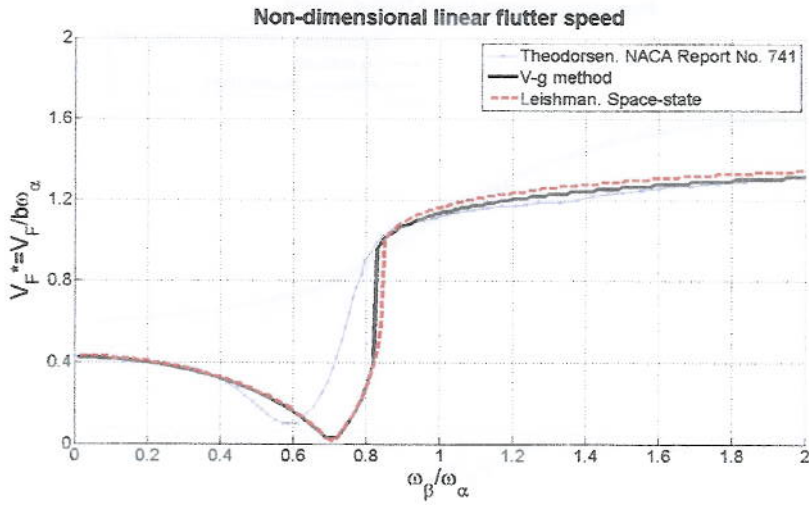


Figure 39: V-g method and Leishman's state-space model against results by Theodorsen and Garrick [23]. $a = -0.2$, $c = 0.6$, $\kappa = 0.2$, $x_\alpha = 0.2$, $r_\alpha^2 = 0.5$, $x_\beta = 0.002$, $r_\beta^2 = 0.002$, $\frac{\omega_h}{\omega_\alpha} = 0.316$

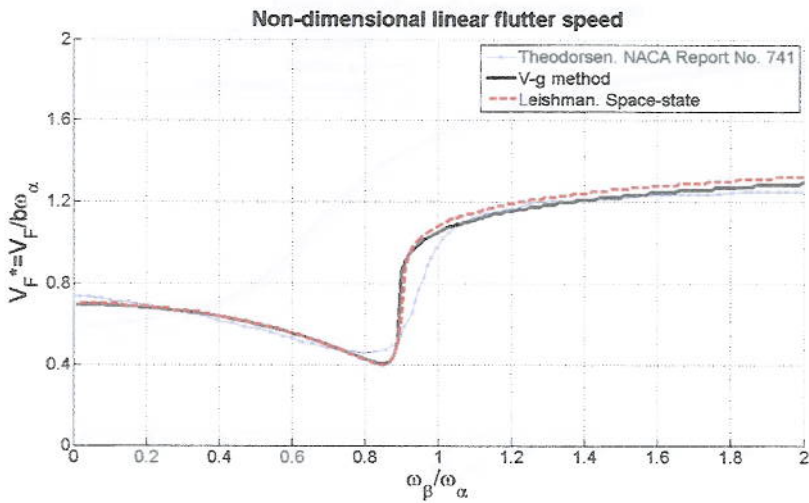


Figure 40: V-g method and Leishman's state-space model against results by Theodorsen and Garrick [23]. $a = -0.2$, $c = 0.6$, $\kappa = 0.2$, $x_\alpha = 0.2$, $r_\alpha^2 = 0.5$, $x_\beta = -0.002$, $r_\beta^2 = 0.002$, $\frac{\omega_h}{\omega_\alpha} = 0.316$

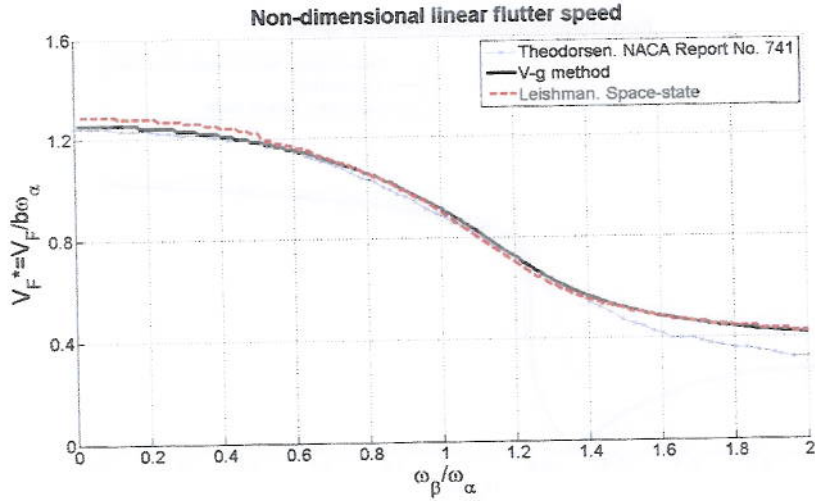


Figure 41: V-g method and Leishman's state-space model against results by Theodorsen and Garrick [23]. $a = -0.2$, $c = 0.6$, $\kappa = 0.2$, $x_\alpha = 0.2$, $r_\alpha^2 = 0.5$, $x_\beta = 0.002$, $r_\beta^2 = 0.002$, $\frac{\omega_h}{\omega_\alpha} = 1$

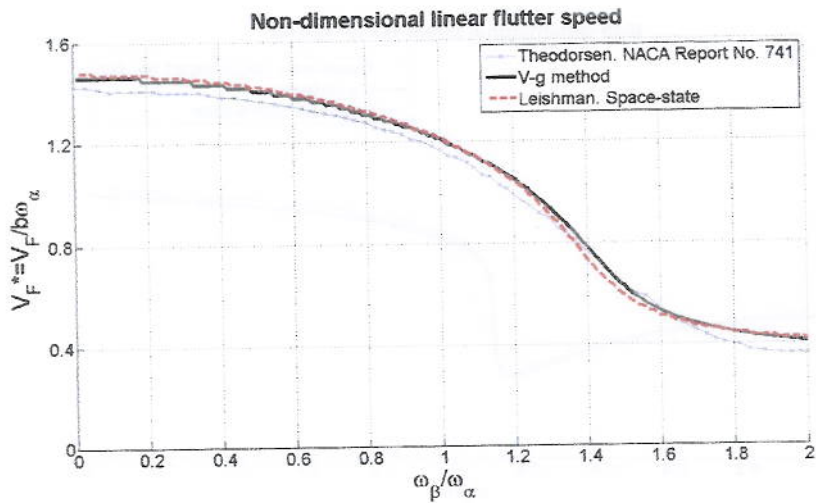


Figure 42: V-g method and Leishman's state-space model against results by Theodorsen and Garrick [23]. $a = -0.2$, $c = 0.6$, $\kappa = 0.2$, $x_\alpha = 0.2$, $r_\alpha^2 = 0.5$, $x_\beta = -0.002$, $r_\beta^2 = 0.002$, $\frac{\omega_h}{\omega_\alpha} = 1$

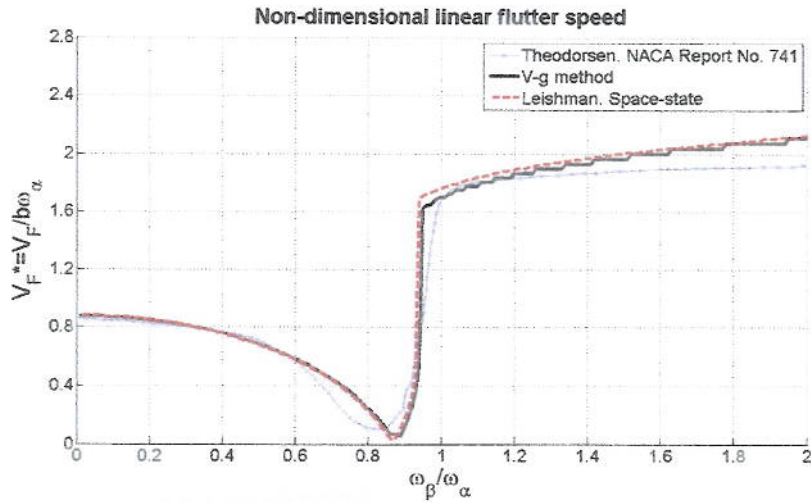


Figure 43: V-g method and Leishman's state-space model against results by Theodorsen and Garrick [23]. $a = -0.2$, $c = 0.6$, $\kappa = 0.083$, $x_\alpha = 0$, $r_\alpha^2 = 0.5$, $x_\beta = 0$, $r_\beta^2 = 0.002$, $\frac{\omega_h}{\omega_\alpha} = 0.607$

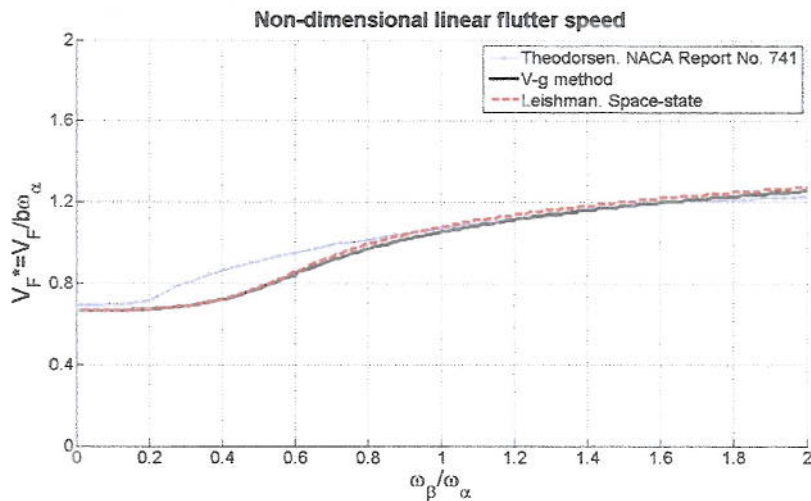


Figure 44: V-g method and Leishman's state-space model against results by Theodorsen and Garrick [23]. $a = -0.4$, $c = 0.6$, $\kappa = 0.25$, $x_\alpha = 0.2$, $r_\alpha^2 = 0.25$, $x_\beta = 0$, $r_\beta^2 = 0.0012$, $\frac{\omega_h}{\omega_\alpha} = 0.25$

AERONAUTICS

24/07/2008

LIBRARY